JADES: measuring reionization properties using Lyman-alpha emission

Gareth C. Jones [1,2,3]★ Andrew J. Bunker,[1] Aayush Saxena [1,4] Santiago Arribas,[5]
Rachana Bhatawdekar,[6,7] Kristan Boyett [1,8,9] Alex J. Cameron [1] Stefano Carniani [10]
Stephane Charlot [11] Emma Curtis-Lake [12] Kevin Hainline,[13] Benjamin D. Johnson,[14]
Nimisha Kumari [15] Michael V. Maseda [16] Hans-Walter Rix,[17] Brant E. Robertson,[18]
Sandro Tacchella [2,3] Hannah Übler [2,3] Christina C. Williams,[19] Chris Willott,[20] Joris Witstok [2,3]
and Yongda Zhu [13]

Affiliations are listed at the end of the paper

ABSTRACT

Lyα is the transition to the ground state from the first excited state of hydrogen (the most common element). Resonant scattering of this line by neutral hydrogen greatly impedes its emergence from galaxies, so the fraction of galaxies emitting Lyα is a tracer of the neutral fraction of the intergalactic medium (IGM), and thus the history of reionization. In previous works, we used early *JWST*/NIRSpec data from the *JWST* Advanced Deep Extragalactic Survey (JADES) to classify and characterize Lyα emitting galaxies (LAEs). This survey is approaching completion, and the current sample is nearly an order of magnitude larger. From a sample of 795 galaxies in JADES at $4.0 < z < 14.3$, we find evidence for Lyα emission in 150 sources. We reproduce the previously found correlation between Lyα escape fraction ($f_{\rm esc}^{\rm Ly\alpha}$) – Ly$\alpha$ rest-frame equivalent width (REW$_{\rm Ly\alpha}$) and the negative correlation between Lyα velocity offset – $f_{\rm esc}^{\rm Ly\alpha}$. Both $f_{\rm esc}^{\rm Ly\alpha}$ and REW$_{\rm Ly\alpha}$ decrease with redshift ($z \gtrsim 5.5$), indicating the progression of reionization on a population scale. Our data are used to demonstrate an increasing IGM transmission of Lyα from $z \sim 14 - 6$. We measure the completeness-corrected fraction of LAEs ($X_{\rm Ly\alpha}$) from $z = 4 - 9.5$. An application of these $X_{\rm Ly\alpha}$ values to the results of previously utilized semi-analytical models suggests a high neutral fraction at $z = 7$ ($X_{\rm HI} \sim 0.8 - 0.9$). Using an updated fit to the intrinsic distribution of REW$_{\rm Ly\alpha}$ results in a lower value in agreement with current works ($X_{\rm HI} = 0.64^{+0.13}_{-0.21}$). This sample of LAEs will be paramount for unbiased population studies of galaxies in the EoR.

Key words: galaxies: high-redshift – intergalactic medium – dark ages, reionization, first stars.

1 INTRODUCTION

It has been well established that early after the Big Bang ($z \sim 1100$, or $t_{\rm H} = 360$ Myr), the Universe cooled enough to permit the formation of neutral hydrogen atoms (i.e. the Epoch of Recombination, e.g. Sunyaev & Zeldovich 1980; Seager, Sasselov & Scott 2000), creating the surface of last scattering (i.e. the cosmic microwave background; CMB) and marking the beginning of an epoch during which most hydrogen in the Universe was neutral (a neutral fraction of hydrogen of unity [$X_{\rm HI} = 1$]). This was followed by 'Cosmic Dawn', when the first stars formed and began to ionize their surrounding gas via ultraviolet (UV) radiation ($z > 10$; see review of Klessen & Glover 2023). The time between the formation of the first stars and when the intergalactic medium (IGM) was fully ionized ($X_{\rm HI} \approx 0$) is the epoch of reionization (EoR). The current general consensus is that the Universe was mostly ionized again by $z \sim 6$ (e.g. Fan et al. 2006; McGreer, Mesinger & D'Odorico 2015; Planck Collaboration XIII 2016); but the discovery of neutral gas 'islands' at later epochs

suggests that the EoR did not conclude until slightly later (e.g. $z \sim 5.2 - 5.3$; Kulkarni et al. 2019; Keating et al. 2020a; Bosman et al. 2022; Becker et al. 2024).

The study of the EoR is one of the major focuses of modern astrophysics, including investigations of the drivers [e.g. active galactic nuclei (AGNs), small/massive galaxies, mergers; Hassan et al. 2018; Naidu et al. 2020; Bosman et al. 2022; Witten, Laporte & Katz 2023; Grazian et al. 2024; Madau et al. 2024] and topology of reionization (e.g. Pentericci et al. 2014), as well as the escape mechanisms of ionizing radiation (e.g. Chisholm et al. 2018). Here, we focus on characterizing the progression of the EoR through measurements of $X_{\rm HI}(z)$.

There are multiple pathways to study the evolution of $X_{\rm HI}$, including damping wing (DW) observations of QSOs (e.g. Bañados et al. 2018; Ďurovčíková et al. 2020; Yang et al. 2020) and galaxies (e.g. Fausey et al. 2024; Hsiao et al. 2024; Umeda et al. 2024), CMB studies (e.g. Planck Collaboration VI 2020), and comparisons of Lyα observations to models (e.g. Mason et al. 2018a; Bhagwat et al. 2024b; Feldmann et al. 2024). This latter path can further be divided into different methods, including studies of the Lyα luminosity function (e.g. Konno et al. 2014; Inoue et al. 2018), clustering of

Lyα-emitting galaxies (LAEs; e.g. Ouchi et al. 2010; Sobacchi & Mesinger 2015; Ouchi et al. 2018), and Lyman forest dark fractions (e.g. Keating et al. 2020b; Bosman et al. 2022; Zhu et al. 2022). Together, these studies suggest an evolution of $X_{HI}(z \gtrsim 13) = 1$ to $X_{HI}(z \sim 5.3) = 0$ with a midpoint of $X_{HI}(z \sim 7) = 0.5$, although the exact shape of this evolution is under debate.

An additional method of characterizing $X_{HI}(z)$ is the study of the evolution of the Lyα emitter fraction ($X_{Ly\alpha}$). Multiple studies have compared observed and model fractions to place constraints from $z \sim 2 - 8$ (e.g. Stark et al. 2010; Stark, Ellis & Ouchi 2011; Curtis-Lake et al. 2012; Ono et al. 2012; Schenker et al. 2012; Caruana et al. 2014; Schenker et al. 2014; Cassata et al. 2015; Furusawa et al. 2016; De Barros et al. 2017; Stark et al. 2017; Goovaerts et al. 2023; Fu et al. 2024). In a previous work (Jones et al. 2024), we utilized low spectral resolution *JWST* (Gardner et al. 2023), near infrared spectrograph (NIRSpec; Jakobsen et al. 2022; Böker et al. 2023) data (PRISM/CLEAR; with spectral resolving power $R \sim 100$) from the first *JWST* Advanced Deep Extragalactic Survey (JADES; Bunker, NIRSPEC Instrument Science Team & JAESs Collaboration 2020; Eisenstein et al. 2023a) data release to estimate $X_{Ly\alpha}$ at $z = 6$ and $z = 7$. While the sample size was relatively small (84 galaxies) and featured a non-standard M_{UV} range ($-20.48 < M_{UV} < -16.33$), our completeness-corrected analysis resulted in a good determination of $X_{Ly\alpha}$, which was used to constrain $X_{HI}(z = 7)$.

The JADES sample has since been combined with other public *JWST* data sets in order to further constrain $X_{Ly\alpha}(z)$ (Nakane et al. 2024; Napolitano et al. 2024), and the results are in agreement with those of Jones et al. (2024). However, the diverse samples of these newer works (i.e. JADES, CEERS, and other programmes) means that the selection function of each sample will be less homogeneous than a single-programme data set. In addition, neither of these works investigated the rest-frame Lyα equivalent width (REW$_{Ly\alpha}$) completeness of their data set, which will result in skewed $X_{Ly\alpha}(z)$ distributions. Here, we exploit the expanded JADES data set to characterize Lyα emission in the early Universe ($4.0 < z < 14.3$; corresponding to $\sim 0.3 - 1.5$ Gyr after the Big Bang).

This work is organized as follows. We discuss our sample in Section 2 and our spectral fitting procedure in Section 3. The correlations from this analysis are explored in Section 4. Section 5 contains a completeness-corrected estimation of the Lyα fraction, which is used to constrain X_{HI} and the IGM transmission of Lyα. We conclude in Section 6.

We assume a standard concordance cosmology throughout: $(\Omega_\Lambda, \Omega_m, h) = (0.7, 0.3, 0.7)$ and use AB magnitudes.

2 SAMPLE

2.1 Observations overview

For this analysis, we use all observed NIRSpec spectroscopy so far from the JADES survey, which spans PID 1180 and 1181 (PI D. Eisenstein), PID 1210, 1286, and 1287 (PI N. Luetzgendorf), and PID 3215 (PIs D. Eisenstein and R. Maiolino). This survey observed galaxies in the Great Observatories Origins Deep Survey (GOODS; Dickinson, Giavalisco & GOODS Team 2003) north (N) and south (S) fields with the *JWST*/NIRSpec Multi-Shutter Array (MSA; Ferruit et al. 2022) in both low (PRISM/CLEAR; spectral resolving power $R \sim 100$) and medium spectral resolution (G140M/F070LP, G235M/F170LP, G395M/F290LP; $R \sim 1000$). Some survey tiers also contain high spectral resolution observations (G395H/F290LP; $R \sim 2700$).

Table 1. JADES tier distribution of the sample analysed in this work. For each survey tier, we also list a shorthand label.

| PID	Field	Tier	Selection	Label	$N_{z>4}$
1180	GOODS-S	Medium	*HST*	1180_MHS	114
1180	GOODS-S	Medium	*JWST*	1180_MJS	92
1181	GOODS-N	Medium	*HST*	1181_MHN	96
1181	GOODS-N	Medium	*JWST*	1181_MJN	126
1210	GOODS-S	Deep	*HST*	1210_DHS	66
1286	GOODS-S	Medium	*JWST*	1286_MJS	209
1287	GOODS-S	Deep	*JWST*	1287_DJS	36
3215	GOODS-S	Deep	*JWST*	3215_DJS	56
				TOTAL:	795

For each JADES tier (see Table 1), a large list of potential target galaxies was aggregated. Each galaxy was given a priority class (PC) dependent on e.g. redshift, *HST* (or *JWST*, if available) colours, and UV brightness (see Bunker et al. 2024; D'Eugenio et al. 2024 for details of PCs), which were used in the construction of MSA masks. This scheme was designed to ensure observations of both extraordinary objects (e.g. GN-z11; Bunker et al. 2023) and a statistically significant number of representative galaxies over the probed range of redshifts. For more details, see the full description of the survey (Eisenstein et al. 2023a) and data release papers (Eisenstein et al. 2023b; Bunker et al. 2024; D'Eugenio et al. 2024). The resulting spectra were visually inspected (D'Eugenio et al. 2024), resulting in precise spectroscopic redshifts for each galaxy. For the two highest redshift sources in the sample, we include the updated redshifts for 183 348 (JADES-GS-z14-0; $z_{sys} = 14.32$) and 20 018 044 in 1287_DJS (JADES-GS-z14-1; $z_{sys} = 13.90$; Carniani et al. 2024). We also adopt the updated redshift for 20 013 731 in 1287_DJS (JADES-GS-z13-1-LA; $z_{sys} = 13.01$) from Witstok et al. (2024a). Due to the spatially extended nature of Lyα emission (e.g. Jung et al. 2024), we use a wide extraction aperture (5 pixels$\sim$ 0.5 arcsec; e.g. Bunker et al. 2023; Curti et al. 2024a; Tang et al. 2024b).

Some targets were observed in multiple tiers due to a desire for a deeper integration or a repeated observation due to previous data being made unusable by an electrical short. To avoid including these observations, we collect all inspected galaxies that are within 0.25 arcsec of each other and exclude the shallower observation.[1] In all cases, the visual spectroscopic redshifts of the repeat observations agree. Since we wish to analyse the R100 data, we exclude observations where the R100 data are corrupted (e.g. due to electrical shorts), resulting in 2992 unique galaxies with good R100 data and precise redshifts. A redshift cut of $z > 4$ is placed, so that we can detect Lyα in the wavelength range of the R100 data. With these limits and exclusions, we find a list of 795 unique galaxies. The distribution of sources between survey tiers is shown in Table 1.

2.2 Galaxy clustering

The galaxies that we analyse in this work have a similar set of selection criteria and a uniform calibration pipeline, making a well-founded statistical analysis possible. The sources are well distributed across the two GOODS fields (Fig. 1), and some galaxies are closely clustered. However, due to the size of each field (~ 18 arcmin, corresponding to ~ 7.5 Mpc at $z = 4$ or ~ 5.2 Mpc at $z = 10$) and

---

[1] While a future data release will include combined spectra from multiple survey tiers, this is not yet available.
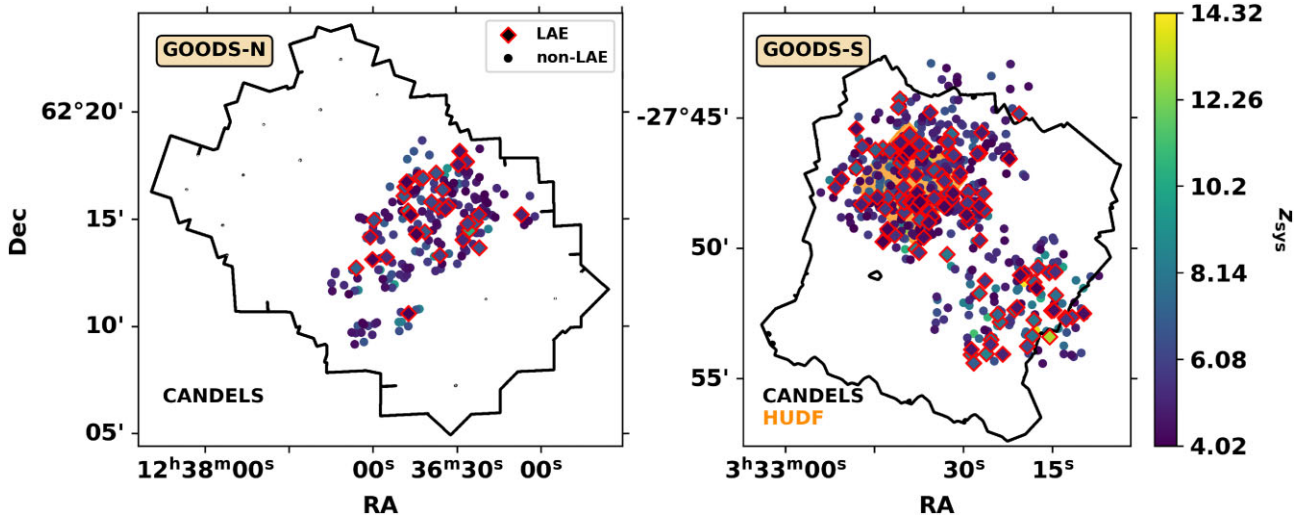
Figure 1. Spatial distribution of our sample, coloured by redshift. Sources not detected in Lyα emission are represented as circles, while LAEs are red-edged diamonds (see Section 3 for more details). For reference, we display the footprints of the Cosmic Assembly Near-infrared Deep Extragalactic Legacy Survey (CANDELS; Grogin et al. 2011) field and the Hubble Ultra Deep Field (HUDF; Beckwith et al. 2006).

the number of targets, this clustering is expected. Indeed, since observation planning software (e.g. Bonaventura et al. 2023) enables efficient observations by creating densely packed MSA slit masks without spectral overlap, we expect a number of galaxies with small projected spatial separations.

Previous studies of the UV luminosity function (e.g. Donnan et al. 2023; Harikane et al. 2023; Robertson et al. 2024) have shown that the density of galaxies for a given $M_{\rm UV}$ decreases at higher redshifts. The sample selection procedure of JADES was designed to maintain a statistical sample across a wide range of redshifts (Bunker et al. 2024; D'Eugenio et al. 2024), and acts to preferentially observe more high-redshift galaxies than would be included in a flux-limited survey (Fig. 2).

Recently, Helton et al. (2024) searched JADES NIRCam (Rieke et al. 2023) data for galaxy overdensities at $4.9 < z_{\rm sys} < 8.9$, finding 17 overdensities in GOODS-N and GOODS-S. By applying the same association criteria as Helton et al. (i.e. projected physical separations of < 0.1 Mpc and velocity offsets of $< 500\,{\rm km\,s^{-1}}$), we find that eight of our 795 galaxies (i.e. ~ 1 per cent) fall into these overdensities (three in JADES-GN-OD-7.144, one in JADES-GS-OD-6.876, two in JADES-GS-OD-7.954, and two in JADES-GS-OD-8.220). Thus, our sample is not strongly affected by high galaxy overdensities. While LAEs have been found in overdensities or close pairs (e.g. Saxena et al. 2023; Witten et al. 2024; Witstok et al. 2024c), the study of LAE clustering is deferred to a future work.

3 SPECTRAL FITTING

Our previous work was focused on REW$_{\rm Ly\alpha}$, and only dealt with on the Lyα line (Jones et al. 2024). In this work, we extend our focus to the Lyα escape fraction ($f_{\rm esc}^{\rm Ly\alpha}$), which requires flux estimates of at least one Balmer line (e.g. Hα or Hβ). Because of this, we extend our spectral fitting to encompass the full wavelength range covered by the PRISM/CLEAR disperser/filter combination (i.e. $0.6 - 5.3\,\mu$m). In addition, we include the higher resolution R1000 data, in order to verify our fits and study relationships with the velocity offset between Lyα and the systemic redshift.

3.1 Model description

The wide wavelength coverage, deep continuum sensitivity, and low spectral resolution of the R100 data mean that an appropriate model of the line and continuum emission requires careful construction. Before modelling each galaxy spectrum, we derive an estimate of $M_{\rm UV}$ by integrating the spectrum between $\lambda_{\rm rest} = 1400 - 1500\,{\rm \AA}$. This range is chosen to overlap with one of the windows of Calzetti, Kinney & Storchi-Bergmann (1994), and avoid contamination by possible CIV$\lambda\lambda 1548, 1551$ emission (e.g. Izotov et al. 2024; Navarro-Carrera et al. 2024). If this $M_{\rm UV}$ estimate has an uncertainty (based on the error spectrum) of < 0.5 magnitude, then we claim that $M_{\rm UV}$ is well determined. Otherwise, we determine a 3σ lower limit on $M_{\rm UV}$ based on the RMS noise level of the observed spectrum (see Appendix A).

The continuum at rest-frame ultraviolet (UV) wavelengths in the early Universe (i.e. at $z \gtrsim 5$) is commonly fit as a power-law model with a slope $\beta_{\rm UV} \sim -2$ (e.g. Yamanaka & Yamada 2019; Cullen et al. 2023; Topping et al. 2024). But previous works (e.g. Jones et al. 2024; Napolitano et al. 2024) suggest that the continuum just redwards of Lyα ($\lambda_{\rm rest} \sim 0.12 - 0.15\,\mu$m) is well-modelled as a power-law function with a slope that may deviate from that of $\beta_{\rm UV}$. Indeed, Cameron et al. (2024) suggest that this deviation in one galaxy is a sign of two-photon nebular continuum emission (e.g. Dijkstra 2009; Katz et al. 2024; but see also Li et al. 2024; Tacchella et al. 2024; Terp et al. 2024 for alternate interpretations), as seen in low-redshift galaxies (e.g. Hall et al. 2004; Johnstone et al. 2012). For sources in the epoch of reionization (and to some degree sources at lower redshift), reservoirs of neutral gas will create DWs (e.g. Mortlock et al. 2011). While the low spectral resolution of the R100 spectra results in the appearance of pseudo-DWs (e.g. Jones et al. 2024), detailed investigations into DWs at high redshift are ongoing (e.g. Fujimoto et al. 2023; Heintz et al. 2024b; Umeda et al. 2024).

With this in mind, we split each spectrum into two models, with a pivot wavelength of $\lambda_{\rm rest} = 0.145\,\mu$m. In the following, we refer to them as the 'R100-blue' and 'R100-red' models. This pivot wavelength is chosen as the middle point of the range we use to derive $M_{\rm UV}$, and is similar to the turnover wavelength of the nebular
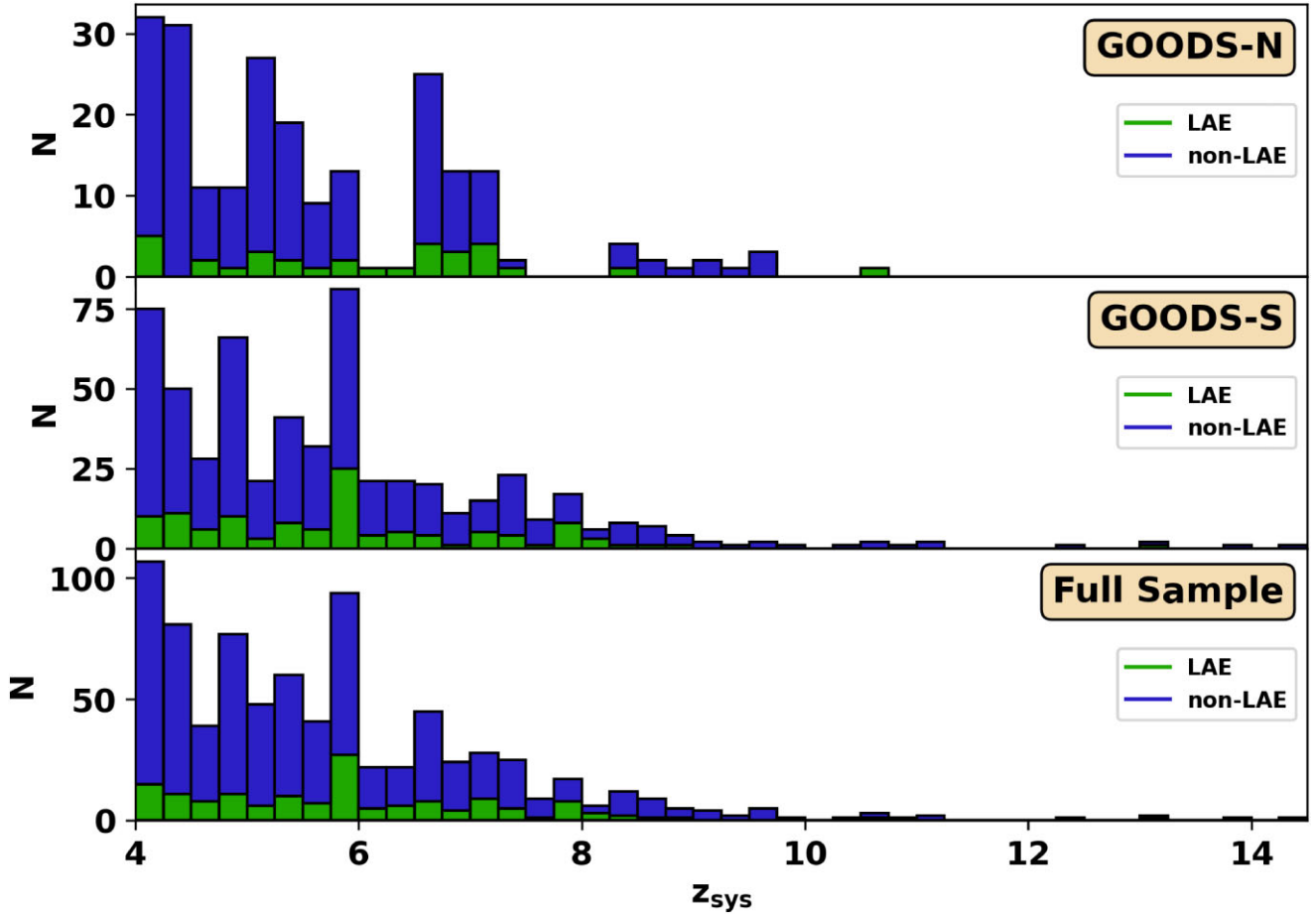
Figure 2. Redshift distribution of sources analysed in this work, coloured by Lyα detection (see Section 3 for more details on fitting procedure).

continuum model of Cameron et al. (2024). The value of each model at the pivot wavelength is fixed to be the mean spectral value of the observed spectrum within $\lambda_{rest} = 1400 - 1500$ Å (i.e. R100-red and R100-blue are required to be continuous), but the models are not assumed to be differentiable.

We first examine the R100-red model, which covers $\lambda_{rest} = 0.145$ μm to $\lambda_{obs} = 5.3$ μm. The continuum of this range is modelled as two power-law segments: one that extends from $\lambda_{obs} \geq (1 + z_{Ly\alpha}) \times 0.145$ μm to the wavelength of Hη ($\lambda_{obs} < (1 + z_{sys})0.3836$ μm), and another that extends from $\lambda_{obs} \geq (1 + z_{sys})0.3836$ μm to the red limit of the spectrum ($\lambda_{obs} = 5.3$ μm). A discontinuity between these segments is allowed, in order to capture a Balmer break or jump. While true Balmer breaks are expected to be more gradual roll-offs marked by numerous absorption lines (e.g. Binggeli et al. 2019; Furtak et al. 2024), the coarse spectral resolution of our data necessitates a simple model. We note that galaxies with high nebular continuum emission may feature Balmer jumps rather than breaks and reddened rest-UV continuum slopes (e.g. Katz et al. 2024; Narayanan et al. 2024; Roberts-Borsani et al. 2024). However, the resulting rest-UV emission may still be described as a power law (e.g. Heintz et al. 2024a). Because our R100-red model contains two segments with separate power-law slopes with no constraints on the sign of the Balmer discontinuity, we may still fit spectra of galaxies with bright nebular continuum emission.

The brightest expected emission lines ([O II]λλ3726, 3729, Hβ, [O III]λλ4959, 5007, Hα, and [N II]λλ6548, 6584)[2] are included via Gaussian model components at the expected wavelengths. We predict the line spread function (LSF) by first taking the fiducial resolving power curve.[3] As noted in de Graaff et al. (2024), this curve was derived assuming that each NIRSpec MSA slit was uniformly illuminated. Since this is not the case for each JADES galaxy, the LSF may be underpredicted. To account for this, we define the width of each Gaussian to be $\sigma_R(\lambda) = F_R\lambda/R(\lambda)/2.355$, where F_R represents the deviation from the fiducial LSF.[4] Using the code PyNeb (Luridiana, Morisset & Shaw 2015) and assuming interstellar medium (ISM) conditions of $T_e = 1.5 \times 10^4$ K and $n_e = 300$ cm^{-3} (e.g. Torralba-Torregrosa et al. 2024), we derive intrinsic ratios of [O III]λ5007/[O III]λ4959= 2.984 and [N II]λ6584/[N II]λ6548= 2.942. [O II]λλ3726, 3729 is treated as a single Gaussian line in the low-resolution R100 data.

---

[2]While the rich JADES data set contains significant emission from many more lines (e.g. Cameron et al. 2024; Laseter et al. 2024; Curti et al. 2024b), we focus on the dominant emission in each spectrum.

[3]As recorded in the *JWST* documentation; https://jwst-docs.stsci.edu/jwst-near-infrared-spectrograph/nirspec-instrumentation/nirspec-dispersers-and-filters

[4]While this deviation has been found to be wavelength dependent, we assume a single average value across the full wavelength range.

The free parameters are thus: the systemic redshift (z_{sys}), the power-law slopes of each of the two continuum components, the normalization of the redder power-law component, the deviation from the fiducial LSF (F_{R}), and the integrated line fluxes of [O II]$\lambda\lambda$3726, 3729, Hβ, [O III]λ5007, [N II]λ6548, and Hα. We use LMFIT (Newville et al. 2014) in 'least_squares' mode to find the best-fitting model. Each spectrum is weighted by its inverse variance, measured from its associated error spectrum. If the initial fit is successful, then the best-fitting line intensities and their uncertainties are inspected. In some cases, the first fit fails due to a non-detection of [O II]$\lambda\lambda$3726, 3729, which is weaker than the other UV/optical lines. To remedy this, we follow failed fits with runs where the [O II]$\lambda\lambda$3726, 3729 intensity is set to 0. There are some galaxies for which we do not detect any significant emission from any of our rest-optical lines, making the measurement of z_{sys} from our data alone impossible. In these cases, we use the visual inspection redshift of D'Eugenio et al. (2024), who used additional emission lines and inspected both the R100 and R1000 spectra. The intensities of lines that are not well detected ($< 3\sigma$) are set to 0, and the fit is repeated until convergence.

Next, we consider the R100-blue model that extends from $\lambda_{\mathrm{obs}} = 0.6\,\mu\mathrm{m}$ to $\lambda_{\mathrm{rest}} = 0.145\,\mu\mathrm{m}$. An initial high-resolution model grid with bins of $0.001\,\mu\mathrm{m}$ is populated with a single power law. A Heaviside step function with a transition at $\lambda_{\mathrm{obs}} = (1 + z_{\mathrm{Ly\alpha}}) \times \lambda_{\mathrm{Ly\alpha}}$ is applied to this model to represent the Lyα break. Some observed spectra feature non-zero emission bluewards of the Lyα break, which may either be incomplete absorption by the intervening Lyα forest (particularly at lower-z) or an artefact introduced during calibration. We account for this by allowing a non-zero continuum level that is constant (in units of F_λ) bluewards of the Lyα break. To introduce Lyα emission, we add flux to the first spectral bin redwards of the Lyα break. The model is then convolved with a Gaussian of width σ_{R}.

If the R100-red model returned a well-determined F_{R} (i.e. $> 3\sigma$), then we adopt this best-fitting value for this model as well. Otherwise, we assume that $F_{\mathrm{R}} = 1$. The free parameters in this model are: $z_{\mathrm{Ly\alpha}}$, the power-law slope of the continuum, and the integrated line flux of Lyα. Again, we use LMFIT in 'least_squares' mode to find the best-fitting model and weigh each spectrum by its inverse variance. To explore the presence of Lyα, we perform initial fits with a variable $F_{\mathrm{Ly\alpha}}$ (considering the line and continuum) and with $F_{\mathrm{Ly\alpha}} \equiv 0$ (continuum-only). If these fits terminate successfully, then the best-fitting values and reduced χ^2 values are inspected. If the line and continuum fit returns a better reduced χ^2, then we present the Lyα properties. Otherwise, we present upper limits on Lyα.

We also examine the R1000 data for each source. All available data (i.e. G140M, G235M, and G395M) are combined in order to create a composite spectrum. The wavelengths ranges around three line complexes are isolated (Lyα, Hβ–[O III]$\lambda\lambda$4959, 5007, and [N II]$\lambda\lambda$6548, 6584–Hα). Each emission line is fit using a 1D Gaussian profile, where we assume the same [O III]$\lambda\lambda$4959, 5007 and [N II]$\lambda\lambda$6548, 6584 ratios as for the R100 fit.

The Lyα emission is modelled as a symmetric Gaussian in the R100 and R1000 data. Other works adopt a more complex asymmetric profile (e.g. Shibuya et al. 2014), due to the relatively high spectral resolving power (i.e. $R > 1000$) of their data (e.g. see works utilizing MUSE, e.g. Kerutt et al. 2022; DEIMOS, e.g. Ono et al. 2012; and MOSFIRE, e.g. Oesch et al. 2015). Because Lyα in our sample is shifted to $\lambda_{\mathrm{obs}} \sim 0.6 - 1.9\,\mu\mathrm{m}$ (with a preponderance of galaxies at the lower edge), our resolving power is $R \sim 30 - 100$ for the R100 data and $R \sim 300 - 800$ for the R1000 data, making it difficult to resolve the true Lyα profile (e.g. Saxena et al. 2024a).

Many properties of the JADES data are described in greater detail in other works, so we will not discuss them here. These include the possibility of Lyα DWs (e.g. Jakobsen et al., in preparation), the presence of damped Lyα systems (e.g. Hainline et al. 2024), UV spectral slopes (Saxena et al. 2024b), and population properties derived from stacked data (Kumari et al. 2024).

3.2 Further observables

The rest-frame equivalent width of each line is calculated using its integrated flux (F_{line}), redshift (z_{sys}), and the continuum model evaluated at the centroid wavelength ($S_{\mathrm{C}}(\lambda_{\mathrm{line}})$):

$$\mathrm{REW}_{\mathrm{Ly\alpha}} = \frac{F_{\mathrm{line}}}{(1 + z_{\mathrm{sys}})S_{\mathrm{C}}(\lambda_{\mathrm{line}})}. \tag{1}$$

The best-fitting continuum model is used to directly determine the Balmer break by taking the ratio of the two best-fitting power-law components of R100-red at their overlapping point.

Using our best-fitting observed Hα and Hβ integrated fluxes from the R100 or R1000 data, we may directly determine the Balmer decrement (e.g. Domínguez et al. 2013):

$$E(B - V)_{\mathrm{BD}} = \frac{2.5}{k(\lambda_{\mathrm{H\beta}}) - k(\lambda_{\mathrm{H\alpha}})} \log_{10}\left(\frac{F_{\mathrm{H\alpha,obs}}/F_{\mathrm{H\beta,obs}}}{2.876}\right), \tag{2}$$

where $k(\lambda)$ is the assumed dust attenuation curve (Calzetti et al. 2000) and we derive an intrinsic $F_{\mathrm{H\alpha}}/F_{\mathrm{H\beta}} = 2.876$ using PyNeb and assuming fiducial ISM conditions of $T_{\mathrm{e}} = 1.5 \times 10^4$ K and $n_{\mathrm{e}} = 300\,\mathrm{cm}^{-3}$ (e.g. Torralba-Torregrosa et al. 2024). This is then used to derive an intrinsic (dust-corrected) Hα integrated flux:

$$F_{\mathrm{H\alpha,int}} = F_{\mathrm{H\alpha,obs}} 10^{k(\lambda_{\mathrm{H\alpha}})E(B-V)_{\mathrm{BD}}/2.5}. \tag{3}$$

Through PyNeb, our ISM condition assumptions yield intrinsic ratios of $F_{\mathrm{Ly\alpha}}/F_{\mathrm{H\alpha}} = 8.789$ and $F_{\mathrm{Ly\alpha}}/F_{\mathrm{H\beta}} = 24.487$, assuming case B recombination. These are combined with the result of equation (3) to derive the intrinsic $F_{\mathrm{Ly\alpha}}$. This is then used to derive the Lyα escape fraction:

$$f_{\mathrm{esc}}^{\mathrm{Ly\alpha}} = F_{\mathrm{Ly\alpha,obs}}/F_{\mathrm{Ly\alpha,int}}. \tag{4}$$

We estimate $f_{\mathrm{esc}}^{\mathrm{Ly\alpha}}$ both by de-reddening Lyα and each Balmer line, and by not correcting for dust (see Section C4).

Due to the wavelength coverage of our R100 observations (i.e. $0.60 - 5.30\,\mu\mathrm{m}$), we may detect H$\alpha$ for galaxies at $z \lesssim 7.1$, Hβ up to $z \lesssim 9.9$, and Lyα for $z \gtrsim 3.9$. The R1000 observations have a slightly smaller wavelength coverage (i.e. $0.70 - 5.10\,\mu\mathrm{m}$), so we may detect H$\alpha$ for galaxies at $z \lesssim 6.8$, Hβ up to $z \lesssim 9.5$, and Lyα for $z \gtrsim 4.8$.

Our R1000 data allow us to determine the Lyα velocity offset with respect to the redshift based on the rest-optical lines (also derived from the R1000 data). The redshift of Lyα emission is measured in two ways: from the centroid of the best-fitting Gaussian model ($\Delta v_{\mathrm{Ly\alpha,G}}$), and from the wavelength corresponding to the peak flux within $[-500, +1000]\,\mathrm{km\,s^{-1}}$ of Lyα ($\Delta v_{\mathrm{Ly\alpha,P}}$). Due to the large size of our sample, these approaches are simpler than that of Saxena et al. (2024a), who fit each R1000 spectrum with asymmetric and symmetric Gaussian models using an MC approach. We will use $\Delta v_{\mathrm{Ly\alpha,P}}$ in the following analyses (see Appendix C3 for a comparison of these velocities).

3.3 Spectral fitting results

As discussed in Section 2, our parent sample contained 795 galaxies with precise spectroscopic redshifts from visual inspection of the

R100 and R1000 spectra ($z = 4.0 - 14.3$; D'Eugenio et al. 2024). Our fitting routine was applied to each galaxy, resulting in estimates on Lyα, rest-optical lines, and continuum emission. There is evidence for Lyα emission from either the R100 or R1000 spectra at $> 3\sigma$ in 150 galaxies. The best-fitting Lyα flux and REW$_{Ly\alpha}$ values are presented in Table B1 for each such source. A set of fit examples are shown in Fig. 3. The R100- and R1000-based quantities are compared in Appendix C. In Section 3.4, we compare our recovered Lyα properties to those of other works that studied the GOODS fields.

3.4 Comparison to previous results

In this work, we present > 100 galaxies at $z > 4$ with evidence for Lyα emission from the current JADES data set. Because these objects are in a well-studied field, some have been previously detected in Lyα emission. Additionally, a portion of these objects have been included in detailed studies (e.g. GN-z11; Bunker et al. 2023) or analyses of populations (e.g. Tang et al. 2024b).

This work is a continuation of a previous study (Jones et al. 2024), which searched for Lyα emission in a sample of 84 galaxies at $5.6 < z < 11.9$ from R100 data in the first JADES data release (1210_DHS, 1180_MHS, and 1286_MJS). Using a similar model as our R100-blue model, they found evidence for Lyα emission in 17 galaxies. All of these sources are recovered in our analysis, with REW$_{Ly\alpha}$ values in agreement (i.e. within 3σ).

Similarly, Saxena et al. (2024a) used R1000 data from 1210_DHS and 1180_MHS to find evidence of Lyα emission in a sample of 17 galaxies at $5.8 < z < 8.0$. For all of the galaxies in 1210_DHS and most of the galaxies in 1180_MHS, our results agree. However, there are some noteworthy exceptions in the medium-tier data. These may be due to different pipeline reductions (in some cases using different calibrations) or different continuum-level assumptions. As part of our effort to avoid including sources twice, we exclude one LAE in 1180_MHS from Saxena et al. (2024a) in favour of a galaxy in 1286_MJS. The two sources have a projected separation of 0.07 arcsec (~ 0.4 kpc at the mean redshift of $z = 6.60$) and $\Delta z = 0.12$ (~ 5000 km s^{-1}). This velocity offset is larger than the threshold used in most merger classification studies (e.g. Ventou et al. 2017; Endsley et al. 2020; Duan et al. 2024), but it is smaller than the threshold of Gupta et al. (2023) for a companion galaxy. An examination of the NIRCam data for these objects shows that they both lie within an extended feature.[5] Since their separation is less than the width of the MSA shutter (0.2 arcsec), we only include the source that was targeted using *JWST*-based selection and astrometry.

Stanway et al. (2004) detected Lyα emission from a source at $z \sim 5.8$ (GOOD-S SBM03#1) with Keck/DEIMOS (REW$_{Ly\alpha}$ = 30 ± 10 Å). This emission is coincident with an LAE in our sample (JADES-GS+53.16685−27.80413 in 3215_DJS, REW$_{Ly\alpha}$ = 51 ± 11 Å). Thus, we identify this LAE as a re-detection of GOOD-S SBM03#1 from the candidate list of Stanway, Bunker & McMahon (2003).

Recently, the highest redshift LAE in our sample (JADES-GS+53.06475−27.89024; $z = 13.01$) was investigated in detail by Witstok et al. (2024b). By applying more detailed continuum models (e.g. two-photon continuum, absorption by damped Lyα absorption systems), they find a larger Lyα flux and intrinsic REW$_{Ly\alpha}$. This

highlights the need for advanced modelling for the highest redshift sources.

Witstok et al. (2025) examine three JADES LAEs that also lie within our sample: JADES-GN+189.19774+62.25696 in 1181_MHN ($z = 8.2790$; called JADES-GN-z8-0-LA), JADES-GS+53.15891−27.76508 in 3215_DJS ($z = 8.4861$; JADES-GS-z8-0-LA), and JADES-GS+53.10900−27.90084 in 1287_DJS ($z = 8.7110$; JADES-GS-z8-1-LA). For each source, our REW$_{Ly\alpha}$ values are in agreement (i.e. within 3σ). The first of these objects was then re-examined by Navarro-Carrera et al. (2024), who find a similar M_{UV}, β_{UV}, and R1000-based Lyα flux and velocity offset as our model, despite using a more detailed asymmetric Gaussian model for Lyα. However, their best-fitting REW$_{Ly\alpha}$ value is $> 7\sigma$ higher than our value due to the use of a best-fitting continuum model from MSAEXP[6] that steeply declines, resulting in a lower expected continuum level and higher REW$_{Ly\alpha}$. Tang et al. (2024a) reported Lyα emission from the $z = 8.4861$ object from Witstok et al. (2025), with comparable R1000-based flux as our value.

Curti et al. (2024a) find tentative evidence for Lyα emission (REW$_{Ly\alpha}$ = 31 ± 16 Å) in the R1000 data of a galaxy (JADES-GS-z9-0) that was observed in two tiers of JADES (1210_DHS and 3215_DJS). This detection was made possible by combining spectra from both programmes, while our analysis of this object only used the higher sensitivity spectra of 3215_DJS (JADES-GS+53.11244−27.77463) and does not show evidence of Lyα emission. So while higher quality spectra may be produced by combining multiple exposures, this process lies beyond the scope of this work.

The well-studied galaxy GN-z11 also lies within our sample (JADES-GN+189.10604+62.24204 in 1181_MJN). The JADES spectra of this source were first presented by Bunker et al. (2023), who find REW$_{Ly\alpha}$ = 18 ± 2 Å using the same extraction aperture (5 pixels) as we use in this work. Our analysis finds the same Lyα flux (i.e. within 1σ), but a lower REW$_{Ly\alpha}$ = 7 ± 2 Å. We find that the Lyα break in the R100 spectrum is well fit by a Heaviside function convolved with the LSF, with no evidence of a strong DW. Because the LSF-convolved spectrum presents a lower value than the intrinsic Lyα continuum level, this discrepancy in REW$_{Ly\alpha}$ is due to different assumptions on the underlying continuum level in our two works.

By combining public data sets from CEERS, JADES, GLASS, and UNCOVER, Tang et al. (2024b) present a set of 210 galaxies at $z > 6.5$. Of these, 110 galaxies are from JADES, and 14 are reported as LAEs. Our independent analysis detects Lyα in 13 of these objects, including the three new LAEs presented in Tang et al. (2024b) but excluding JADES-28342 (GN+189.22436+62.27561).[7] The majority of our REW$_{Ly\alpha}$ values agree (i.e. within 3σ), with the exception of two sources where our REW$_{Ly\alpha}$ values are higher (JADES-GN+189.14579+62.27332 and JADES-GS+53.14555−27.78380) and one source where our REW$_{Ly\alpha}$ value is lower (JADES-GS+53.13347−27.76037).

Finally, we note that our REW$_{Ly\alpha}$ values were measured with the *JWST*/NIRSpec MSA, which uses small observational slits (0.20 arcsec × 0.46 arcsec, where 0.1 arcsec $\lesssim 0.7$ kpc at $z \geq 4$). This is vital, as some studies have reported mismatched *JWST*/NIRSpec MSA and ground-based estimates of Lyα flux (e.g. Jiang et al. 2024;

---

[5] https://jades.idies.jhu.edu/?ra=53.1374139&dec=-27.7652125&zoom=12, see Figure D1.

[6] https://github.com/gbrammer/msaexp

[7] The Lyα emission of this source was only detected in the R1000 data of Tang et al. (2024b), but our analysis pipeline did not return an acceptable R1000 spectrum.
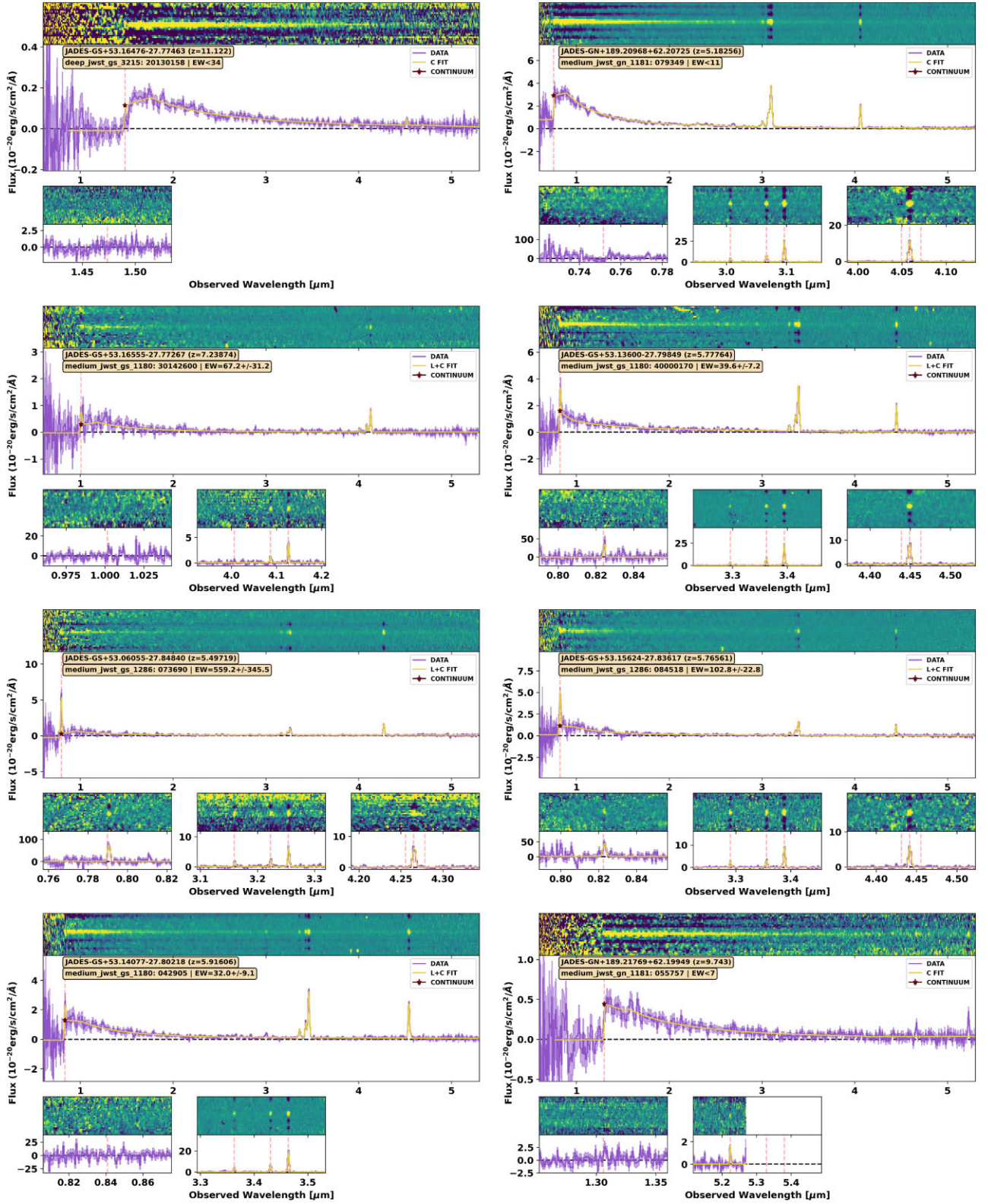
Figure 3. Examples of fitting a line + continuum model to observed JADES data for the full R100 data (upper panel) and portions of the R1000 data (lower panels). In each, we show the observed 2D and 1D spectra. For the 1D spectra, we plot the observed spectrum (purple line) with an associated 1σ error (shaded region). The best-fitting model, which includes the effects of the LSF, is shown by a yellow line. The continuum value at the redshifted Lyα wavelength in the R100 data is represented by a brown star. The 2D corresponding spectrum of each spectrum is shown above each 1D spectrum. We show examples of sources where Lyα is detected in both data sets/neither data set/one data set.
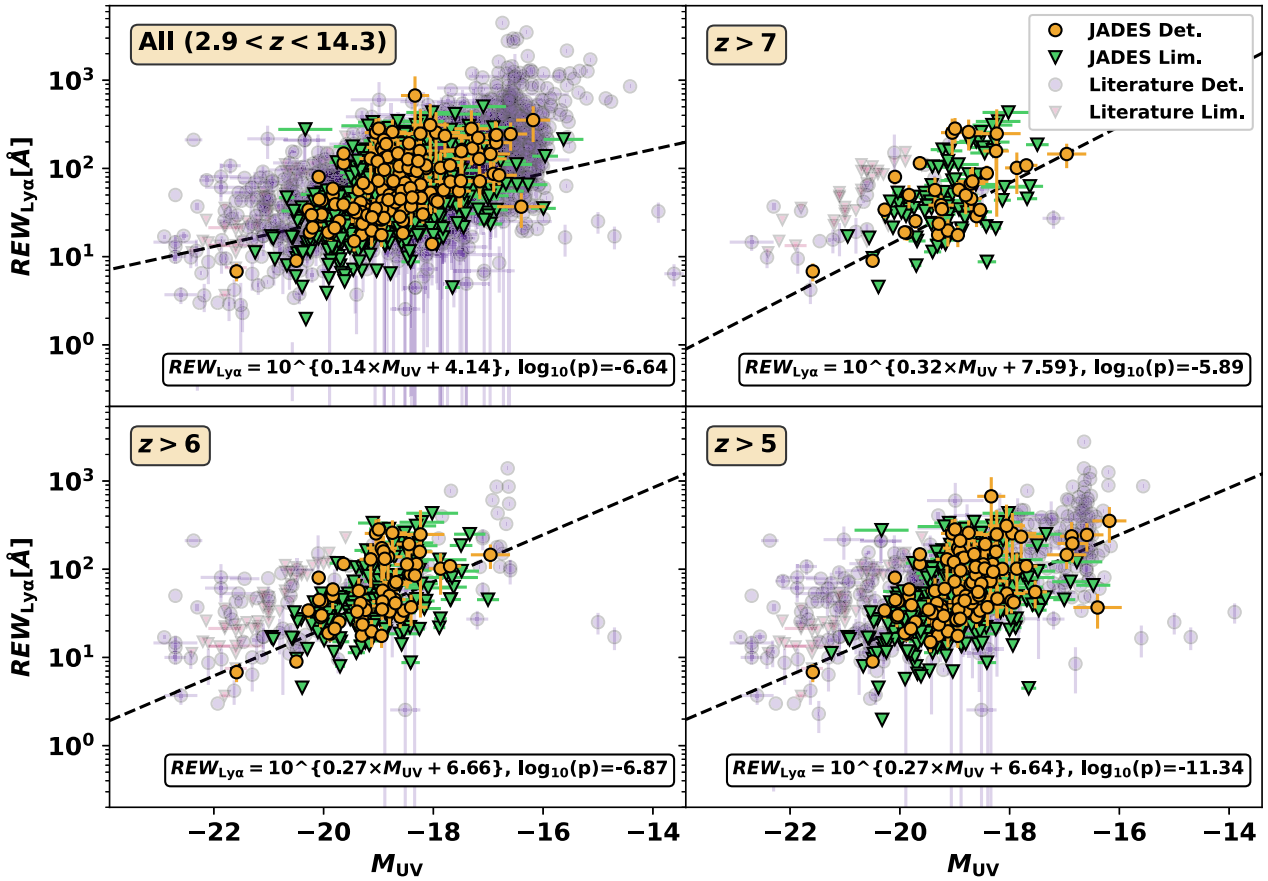
Figure 4. Distribution of rest-frame Lyα equivalent widths as a function of M_{UV} for our sample (orange circles for detections and green triangles for 3σ upper limits) and from literature (purple circles for detections and red triangles for 3σ upper limits). Only sources with robust M_{UV} estimates are shown. An illustrative fit to the JADES detections is shown by the black dashed line, and the best-fitting parameters of this fit are included to the lower right of each panel. The literature sample (spanning a redshift range of $2.9 < z < 8.7$) is taken from a number of works (Cuby et al. 2003; Vanzella et al. 2011; Ono et al. 2012; Schenker et al. 2012; Willott et al. 2013; Song et al. 2016; Pentericci et al. 2018; Shibuya et al. 2018; Hoag et al. 2019; Fuller et al. 2020; Tilvi et al. 2020; Endsley et al. 2022; Jung et al. 2022; Kerutt et al. 2022; Tang et al. 2023) as compiled by Jones et al. (2024).

Jung et al. 2024), which are hypothesized to be due to the small area of the MSA slit, UV-Lyα offset, or the existence of Lyα haloes. Simulations have also confirmed that these effects may result in inaccurate estimates of Lyα flux and equivalent width from slit-based observations (Bhagwat et al. 2024a). Future comparison of our values to ground-based observations should take this effect into account.

## 4 SAMPLE CORRELATIONS

4.1 REW$_{Lyα}$–M_{UV} distribution

The resulting distribution in REW$_{Lyα}$ and M_{UV} is displayed in Fig. 4. As found in other studies (e.g. Fu et al. 2024; Nakane et al. 2024; Napolitano et al. 2024), there is a correlation between these values that is present at all redshift bins, implying that UV-faint galaxies feature higher REW$_{Lyα}$. Previous studies have suggested that this might be due to sensitivity effects (e.g. Jones et al. 2024), as the low Lyα flux of galaxies in the lower right quadrant would require a deep blind survey to detect. But UV-bright, high-REW$_{Lyα}$ galaxies (upper right quadrant), which would be easily detected, are not found. This suggests that the correlation is physical.

4.2 M_{UV}–z distribution

We also present the M_{UV}–z distribution of our sample in Fig. 5. While we exclude sources where M_{UV} was not significantly measured from the R100 spectra, the resulting distribution features a wide range of M_{UV} values (i.e. from ~ -15.5 to ~ -21.75 with a mean of ~ -18.75) and redshifts ($z \sim 4.0 - 14.5$). We note the presence of four extraordinary objects: the UV-bright $z \sim 10.6$ source GNz-11 (lime green point at centre top of plot; Bunker et al. 2023), a verified LAE at $z \sim 13$ (JADES-GS-z13-1-LA; Witstok et al. 2024b), and two of the highest redshift spectroscopically confirmed galaxies to date (JADES-GS-z14-0 and JADES-GS-z14-1; Carniani et al. 2024), which do not exhibit Lyα emission.

Compared to the distribution from the previous work analysing Lyα in JADES (Jones et al. 2024), we can immediately notice some improvements. First, our sample size is $\sim 10\times$ the size of the previous work, due to the inclusion of data from additional JADES tiers and a wider redshift limit ($z > 4$ rather than $z > 5.6$). This results in a more symmetric distribution of M_{UV} values around $M_{UV} \sim -19$ and a larger number of sources in each redshift bin. The LAEs (black-outlined markers) are not clustered in a specific region of the distribution, but include UV-faint and UV-bright galaxies at nearly all redshifts.
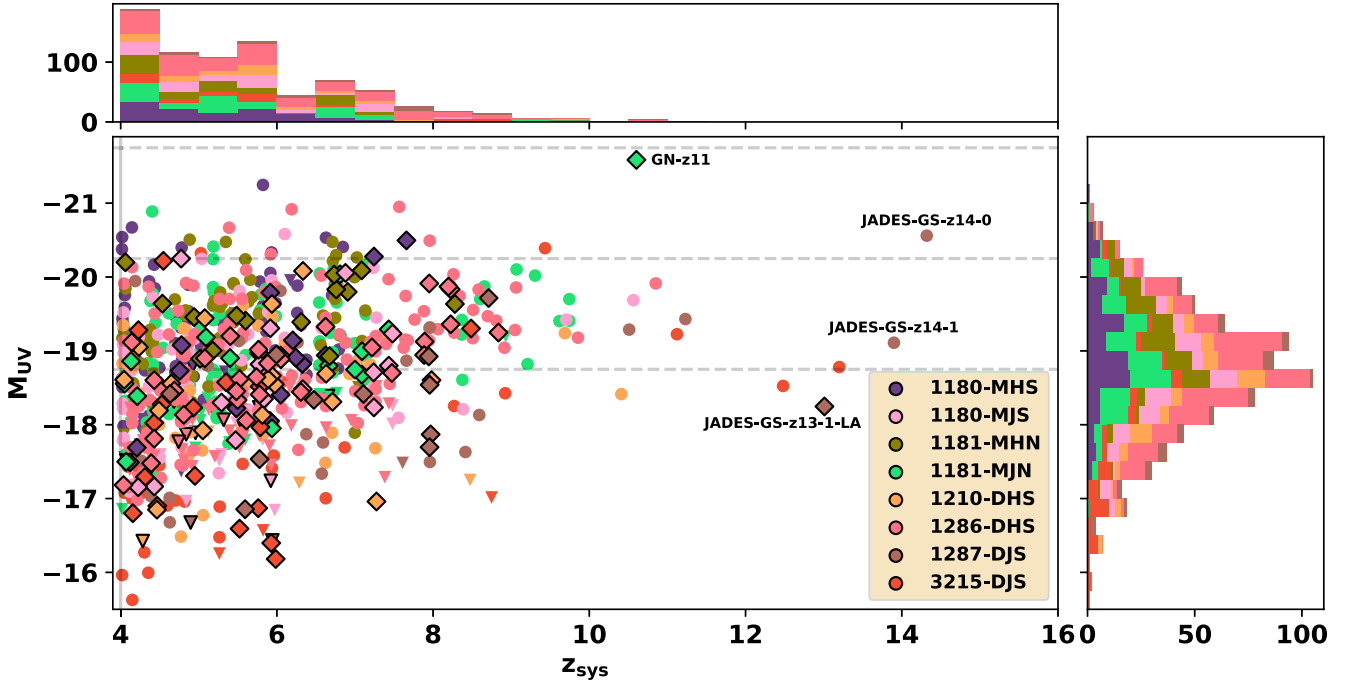
Figure 5. M_{UV} (from NIRSpec R100 spectra) versus systemic redshift (based on rest-frame optical lines) for our sample. Galaxies observed in different tiers are coloured differently. Sources detected in Lyα emission (in R100 and/or R1000) are shown as diamonds with black outlines. Horizontal dashed lines show M_{UV} values of -21.75, -20.25, and -18.75, while the vertical grey line shows our lower redshift cutoff ($z_{sys} > 4.0$). The locations of several well-studied objects are marked: GNz-11 (Bunker et al. 2023), JADES-GS-z13-1-LA (Witstok et al. 2024b), JADES-GS-z14-0, and JADES-GS-z14-1 (Carniani et al. 2024). For sources where M_{UV} is not robustly measured from the observed R100 spectrum, the 3σ lower limit on M_{UV} is shown by a downwards-facing triangle.
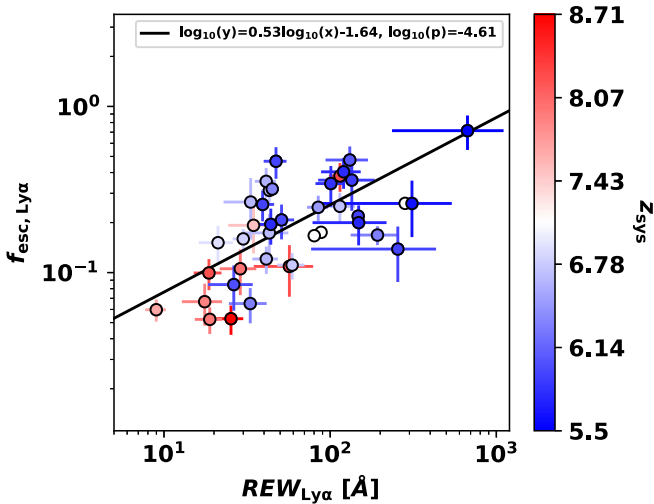
Figure 6. Lyα escape fraction (derived by comparing the observed and intrinsic Lyα/Hβ flux ratio for the R1000 data, using no dust correction) as a function of REW$_{Lyα}$ (derived using the Lyα flux and z_{sys} from R1000 data and the continuum value from R100 data). Each point is coloured by redshift. More details about the use of these values are given in Appendix C4.
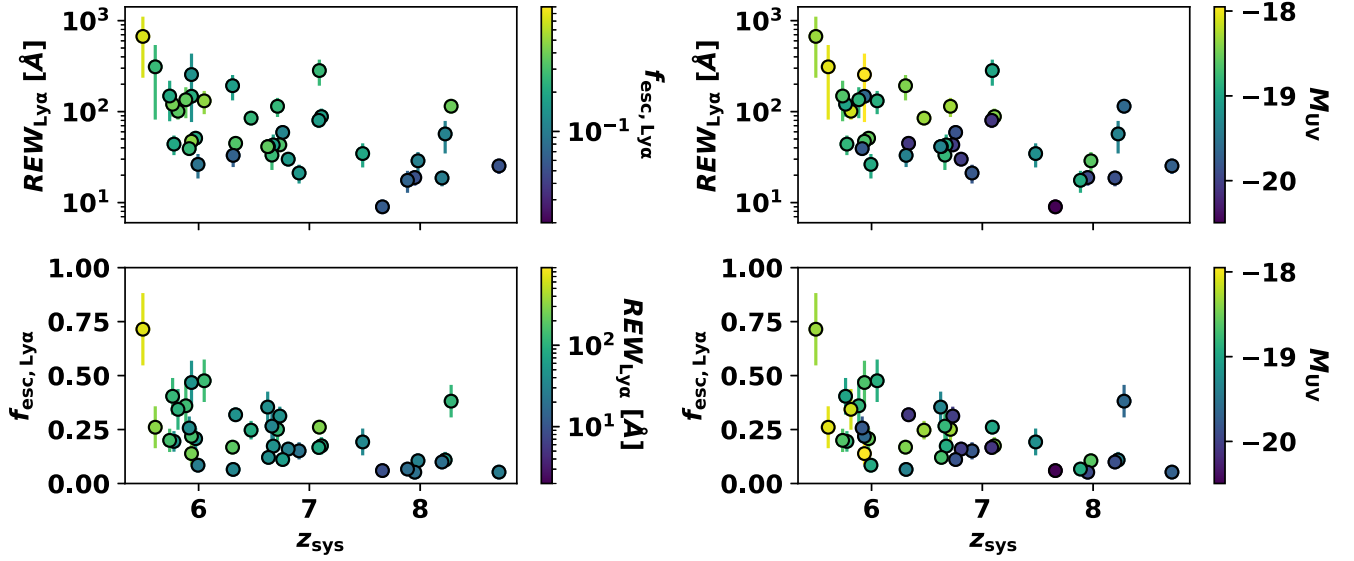
4.3 Lyα escape fraction correlations

We may now consider the larger subsample of all galaxies with measures of Lyα and Hβ in R1000, in order to examine the full relation between $f_{esc}^{Lyα}$ and REW$_{Lyα}$ for our sample (Fig. 6; see Appendix C4 for additional details on our $f_{esc}^{Lyα}$ calculation). The positive correlation, which has been previously evidenced through observations and simulations (e.g. Sobral & Matthee 2019; Cassata

et al. 2020; Roy et al. 2023; Begley et al. 2024; Choustikov et al. 2024) is strengthened by this work with the addition of more galaxies. In addition, it is clear that there is a gradient in redshift, with higher redshift sources showing lower REW$_{Lyα}$ values (e.g. Saxena et al. 2024a).

This is shown more clearly in Fig. 7, where we display REW$_{Lyα}$ and $f_{esc}^{Lyα}$ as functions of redshift. Both quantities decrease with increasing redshift. One may interpret the increasing Lyα escape fraction with cosmic time as a direct sign of the evolution of reionization between $t_H \sim 0.4 - 1.2$ Gyr ($z = 10 - 5$), but it is important to rule out the possibility of selection biases. First, we consider the possibility that due to sensitivity effects, we may be biased towards more extreme systems at high redshift. But since the highest redshift sources have low REW$_{Lyα}$, this is not the case. Alternatively, Saxena et al. (2024a) find that this evolution may be caused by a relation between REW$_{Lyα}$ and M_{UV}, with UV-fainter galaxies exhibiting higher REW$_{Lyα}$. This relation was examined in Section 4.1, where we are not able to discern if it is true or caused by selection effects. Our sample does not have a strong dependence of M_{UV} on redshift (see Fig. 5), and there is no clear gradient in REW$_{Lyα}(z)$ or $f_{esc}^{Lyα}$ with respect to M_{UV} (right panels of Fig. 7), so this is unlikely.

Next, we examine the distribution of $f_{esc}^{Lyα}$ as a function of the Lyα velocity offset $\Delta v_{Lyα}$. Past works (e.g. Tang et al. 2023; Saxena et al. 2024a) found a negative correlation between $\Delta v_{Lyα}$ and $f_{esc}^{Lyα}$, which is reproduced in our data (Fig. 8). This implies that galaxies with high Lyα escape feature Lyα emission near the systemic redshift, which may be caused by a large ionized bubble (e.g. Witstok et al. 2024b). An ionized bubble would enable Lyα to emerge largely unattenuated even at the core of the line. But in systems with neutral gas around the galaxy (i.e. small bubbles), this emission from the line core would be depleted through resonant scattering, with only photons in the red

Figure 7. Redshift evolution of $REW_{Ly\alpha}$ (top row) and Lyα escape fraction (lower row). In the left column, $REW_{Ly\alpha}$ and Lyα escape fraction points are coloured by each other. The right-hand panels instead colour each point by M_{UV}.
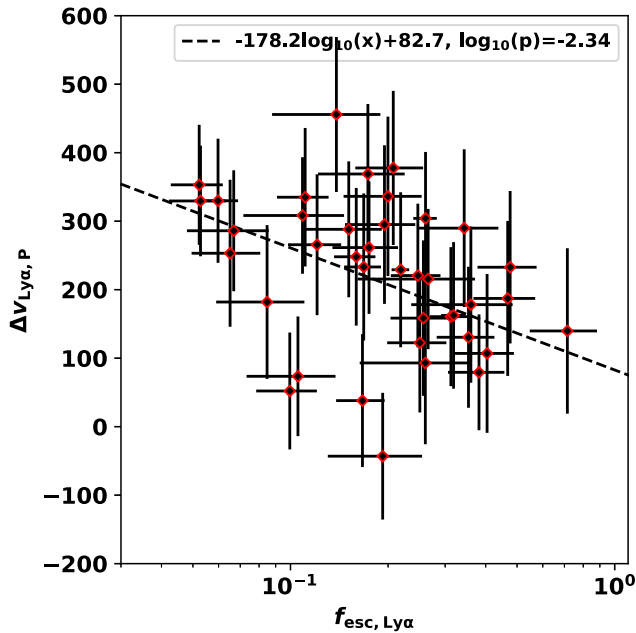

Figure 8. Correlation between $\Delta v_{Ly\alpha}$ and Lyα escape fraction. We plot the best-fitting linear relation and list the relation and *p*-value in the legend.

wings of the line emerging (and consequently a suppressed flux and lower $f_{esc}^{Ly\alpha}$).

4.4 Dust properties

While not the primary focus of this work, we may also inspect the dust properties of the LAEs in our sample. To do this, we compare the rest-UV slope β_{UV} and B–V colour excess $E(B-V)$ from the R100 fits (Fig. 9). The latter is calculated using the observed Balmer decrement (see Section 3.2) and represents the reddening of the nebular lines, which may differ from the reddening of the stellar
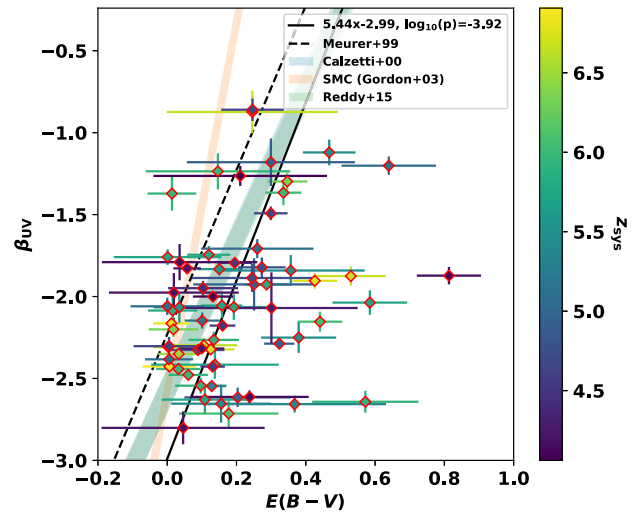
Figure 9. UV spectral slope as a function of B–V colour excess (based on Balmer decrement) for LAEs, where both values are measured from the R100 spectra. Each point is coloured by spectroscopic redshift (also visually validated; D'Eugenio et al. 2024). For comparison, we plot the relations from Reddy et al. (2018) for multiple dust attenuation laws (Meurer, Heckman & Calzetti 1999; Calzetti et al. 2000; Gordon et al. 2003; Reddy et al. 2015). Note that the relations of Calzetti et al. (2000) and Reddy et al. (2015) are very similar, and overlap.

continuum. Our values are in agreement with the stacking analysis of Kumari et al. (2024).

Redder UV slopes can be associated with increased dust extinction (e.g. Bhatawdekar & Conselice 2021), decreased LyC escape (e.g. Chisholm et al. 2022), higher Balmer break (e.g. Langeroodi & Hjorth 2024), and generally increased dust content (e.g. Austin et al. 2024). On the other hand, $E(B-V)$ is a direct measure of dust attenuation (e.g. Domínguez et al. 2013; Matthee et al. 2023). Thus, it is expected that the two parameters should be correlated (e.g. Chisholm et al. 2022). Indeed, we find a positive correlation (Fig. 9).

To put this result in context, we also plot the relations from Reddy et al. (2018) between UV spectral slope and $E(B - V)$ using several dust attenuation laws. The Calzetti et al. (2000), Gordon et al. (2003), and Reddy et al. (2015) relations are calculated using two models: 'Binary Population and Spectral Synthesis' (BPASS; Eldridge & Stanway 2012; Stanway, Eldridge & Becker 2016) with low metallicity (0.14 solar) and those of Bruzual & Charlot (2003, BC03) with 1.4 solar metallicity. The span of these models is shown by a shaded region for each attenuation law. We also include the correlation of Meurer et al. (1999).

The relation that we find for our LAEs features a similar slope as those of Meurer et al. (1999), Calzetti et al. (2000), and Reddy et al. (2015), but with a lower value of β when $E(B - V) = 0$. On the other hand, the SMC curve of Gordon et al. (2003) differs significantly. Because the calculation of our $E(B - V)$ values included the assumption of a Calzetti et al. (2000) attenuation law, this agreement is not surprising. The resulting shift between our correlations and the others could be caused by differences in galaxy properties [e.g. Reddy et al. (2015) use galaxies at $1.5 \leq z \leq 2.5$ while our sample is $4 \leq z \leq 14$] or model assumptions. Further studies will shine more light on the dust properties of high-redshift LAEs.

5 DISCUSSION

5.1 IGM transmission

Following other recent studies (Mason et al. 2018a; Nakane et al. 2024; Tang et al. 2024b), we may use our full distribution of $REW_{Ly\alpha}$ values and upper limits to constrain the redshift evolution of a physical tracer of reionization. While other works examine the neutral hydrogen fraction directly, we will examine the IGM transmission of Lyα (T_{IGM}).

This is possible because of a few basic assumptions that are made in each of the other works. First, we assume that the continuum emission underlying Lyα emission is not extincted. This allows us to calculate an observed $REW_{Ly\alpha,obs.} = T_{IGM}REW_{Ly\alpha,emit.}$. Next, we choose the redshift range of $4.9 < z < 6.5$ (hereafter denoted as $z \sim 5$) as reference[8] and assume that the distribution of $REW_{Ly\alpha,emit.}$ values does not change between $5 < z < 14$. Finally, we assume that this $REW_{Ly\alpha,obs.}$ distribution only changes because of an evolving T_{IGM}.

5.1.1 *REW_{Lyα} distribution*

To begin, we follow a method similar to that of Tang et al. (2024a) to derive the distribution of $REW_{Ly\alpha,emit.}$ values at $z \sim 5$. This is done by isolating all galaxies in our sample that fall into the redshift range and have a well-determined M_{UV} value (see Appendix A). For all such galaxies with Lyα detections, we calculate the probability distribution implied by the $REW_{Ly\alpha}$ value:

$$P_{i,\text{det}}(REW_{Ly\alpha}) = \frac{1}{\sqrt{2\pi}\sigma_i} \exp\left[\frac{-(REW_{Ly\alpha,i} - REW_{Ly\alpha})^2}{2\sigma_i^2}\right], \quad (5)$$

where $REW_{Ly\alpha,i}$ is the measured $REW_{Ly\alpha}$ value and σ_i is the associated uncertainty. For all galaxies that meet the z and M_{UV}

---

[8]This epoch contains the end of the EoR ($T_{IGM} = 1.0$; e.g. Bosman et al. 2022), but also contains a time range where $T_{IGM} < 1.0$. Because of this, we use the $REW_{Ly\alpha}$ distribution as a reference to see how T_{IGM} evolves with z rather than exploring the absolute value of T_{IGM}.

---

constraints but are non-detected in Lyα emission, we find the probability distribution implied by the upper limit on $REW_{Ly\alpha}$:

$$P_{i,\text{lim}}(REW_{Ly\alpha}) = \frac{1}{\sqrt{2\pi}\sigma_i} \exp\left[\frac{-REW_{Ly\alpha}^2}{2\sigma_i^2}\right]. \quad (6)$$

All $P_i(REW_{Ly\alpha})$ values are summed and the resulting distribution is normalized. To ease further computation, we fit the distribution with a log-normal model:

$$P(REW_{Ly\alpha}) = \frac{1}{\sqrt{2\pi}\sigma REW_{Ly\alpha}} \exp\left[\frac{-(\ln(REW_{Ly\alpha}) - \mu)^2}{2\sigma^2}\right]. \quad (7)$$

Using the OPTIMIZE.CURVE_FIT task of SciPy (Virtanen et al. 2020), we find best-fitting values of $\mu = 2.44 \pm 0.01$ and 1.64 ± 0.01. These are comparable to those of Tang et al. (2024b), who used a similar redshift range[9]: $\mu = 2.38^{+0.28}_{-0.31}$ and $\sigma = 1.64^{+0.23}_{-0.19}$.

5.1.2 *IGM transmission calculation*

With a $REW_{Ly\alpha}$ distribution in hand, we employ the Bayesian framework of Mason et al. (2018a) to constrain T_{IGM}. In the case of LAEs, we have measured $REW_{Ly\alpha}$ values (REW_i) and uncertainties (σ_i), which we may use to calculate the likelihood implied by our measurement ($REW_i \pm \sigma_i$):

$$P(REW_i)_{\text{det}} = \int_0^\infty \frac{1}{\sqrt{2\pi}\sigma_i} e^{-(REW - REW_i)^2/(2\sigma_i^2)} \times P(REW/T_{IGM}) \, dREW. \quad (8)$$

For galaxies that are not detected in Lyα emission, we may use our observational 1σ limits on $REW_{Ly\alpha}$ (σ_i) to find the $REW_{Ly\alpha}$ likelihood:

$$P(REW_i)_{\text{lim}} = \int_0^\infty \frac{1}{2}\text{erfc}\left[\frac{REW - 3\sigma_i}{\sqrt{2}\sigma_i}\right] \times P(REW/T_{IGM}) \, dREW. \quad (9)$$

All of these distributions are then combined to create a probability distribution for T_{IGM}:

$$P(T_{IGM}) = \prod_i^N P(REW_i), \quad (10)$$

where $P(EW_i)$ is the $REW_{Ly\alpha}$ probability distribution for each galaxy.

Our sample is separated into three redshift bins ($6.5 < z < 8.0$, $8.0 < z < 10.0$, $10.0 < z < 13.3$), and we exclude galaxies where M_{UV} was not well determined from the R100 data. For each bin, we calculate $P(T_{IGM})$ for $T_{IGM} = [0.01, 0.02, 0.03, \ldots, 1.0]$ and calculate the 16th, 50th, and 84th percentiles, which we present in Fig. 10. This analysis results in similar constraints on T_{IGM} as Tang et al. (2024b).

5.2 Lyα fraction

The large size of our sample allows for new constraints on the Lyα emitter fraction (X_{Lya}). This value represents the fraction of galaxies in an M_{UV} and redshift bin that are detected in Lyα emission with an $REW_{Ly\alpha}$ value greater than a limit. The standard $REW_{Ly\alpha}$ limits are 25, 50, and 75 Å, although some studies use slightly different values (e.g. 10 Å, 55 Å; Stark et al. 2011; Ono et al. 2012; Nakane et al.

---

[9]The different levels of uncertainty originate from different methods of fitting.
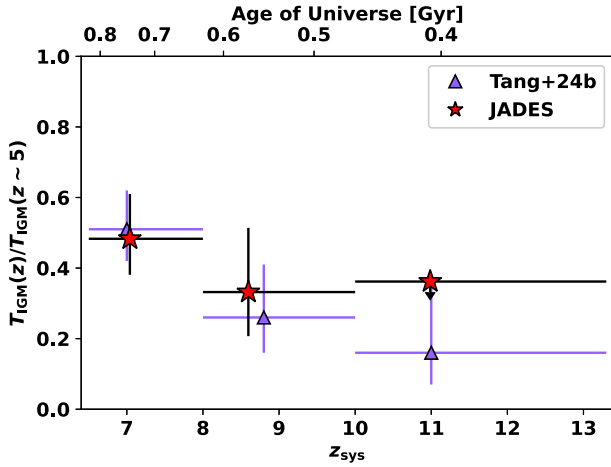
Figure 10. Redshift evolution of IGM transmission of Lyα (with respect to its value at $z \sim 5$), as measured by Tang et al. (2024b) and through our analysis. Both studies show a strong increase in transmission with cosmic time.

2024). Here, we determine $X_{\mathrm{Lya}}(z)$ of our sample, after accounting for incompleteness at low $\mathrm{REW}_{\mathrm{Ly}\alpha}$ values.

5.2.1 Completeness analysis

As in Jones et al. (2024), the galaxies in our sample span a wide range of redshifts and M_{UV} values. In order to use our measurements of $\mathrm{REW}_{\mathrm{Ly}\alpha}$ to place constraints on the characteristics of galaxy populations, we must examine the completeness of our sample at low values of $\mathrm{REW}_{\mathrm{Ly}\alpha}$, where a weak Lyα feature may be washed out by the strong spectral break at this wavelength at the low spectral resolution of the R100 data. But since $\mathrm{REW}_{\mathrm{Ly}\alpha}$ is a function of both the underlying continuum strength (i.e. M_{UV}) and the Lyα flux (in the case of a detection) or the error spectrum (for non-detections), we will use a series of models that take this complexity into account to determine the completeness.

There are a few key points that must be included. First, the sensitivity to Lyα is dependent on both the observed wavelength of the line and the redshift, as the error spectrum for any given NIRSpec observation is not flat. More importantly, the scaling of these error spectra vary from tier to tier, with nearly an order of magnitude difference between the error spectrum of 1180_MHS and 3215_DJS at $\lambda_{\mathrm{obs}} \sim 1\,\mu\mathrm{m}$. In addition, our sample covers a range of $\Delta M_{\mathrm{UV}} > 5$ mag, strongly affecting our ability to detect low $\mathrm{REW}_{\mathrm{Ly}\alpha}$ emission.

An added complexity arises from the fact that we wish to examine the completeness of our sample for all $\mathrm{REW}_{\mathrm{Ly}\alpha}$ values beyond a lower limit, rather than the completeness at a single value. Thus, if we wish to evaluate the completeness value for a single galaxy at a given limit (e.g. > 25 Å), we must create a series of models with a range of $\mathrm{REW}_{\mathrm{Ly}\alpha}$ values and calculate the fraction of models with an intrinsic $\mathrm{REW}_{\mathrm{Ly}\alpha}$ larger than the limit that are well-fit. Assuming a single value (e.g. the $\mathrm{REW}_{\mathrm{Ly}\alpha}$ limit; Jones et al. 2024) will result in an unrealistically low completeness value. Similarly, assuming a uniform $\mathrm{REW}_{\mathrm{Ly}\alpha}$ distribution is nonphysical, as there are fewer extreme LAEs (e.g. Tang et al. 2024a). We choose to use a physically motivated distribution of $\mathrm{REW}_{\mathrm{Ly}\alpha}$ models.
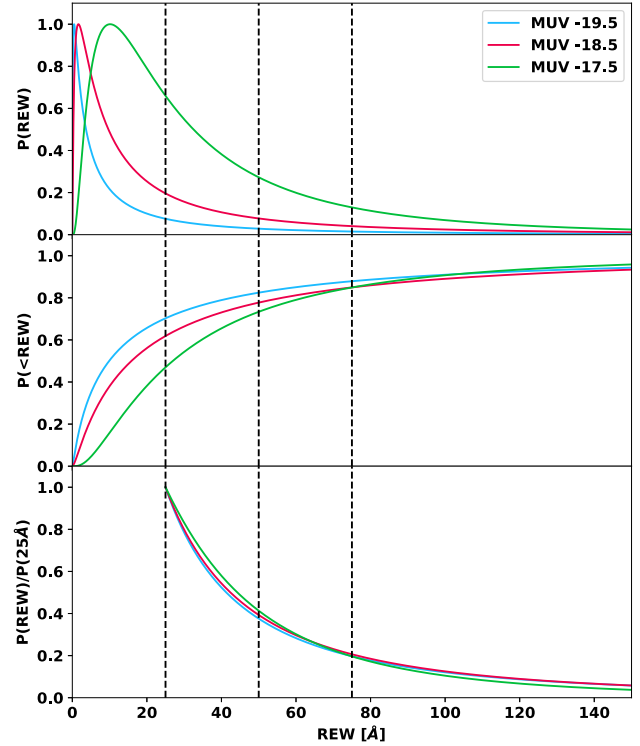
Figure 11. Expected $\mathrm{REW}_{\mathrm{Ly}\alpha}$ distribution of galaxies at $z = 5 - 6$, based on models of Tang et al. (2024a). The top row shows the normalized distribution of galaxies as a function of $\mathrm{REW}_{\mathrm{Ly}\alpha}$, while the middle row shows the CDF. The bottom row shows the same distributions as the top row, but normalized by their value at $\mathrm{REW}_{\mathrm{Ly}\alpha} = 25$ Å. For each panel, we show three M_{UV} values ($M_{\mathrm{UV}} = [-19.5, -18.5, -17.5]$) with different colours, and mark three $\mathrm{REW}_{\mathrm{Ly}\alpha}$ values of interest ($\mathrm{REW}_{\mathrm{Ly}\alpha} = [25, 50, 75]$ Å).

The redshift range $z = 5 - 6$, which lies below the expected midpoint of reionization, can be used to get a handle on the intrinsic distribution of $\mathrm{REW}_{\mathrm{Ly}\alpha}$ at high redshift without much impact from IGM absorption. The $\mathrm{REW}_{\mathrm{Ly}\alpha}$ distribution of galaxies in this epoch was recently determined by Tang et al. (2024a) for three bins of $M_{\mathrm{UV}} = [-17.5, -18.5, -19.5]$. Because their analysis already accounts for completeness, it is suitable for this analysis. This distribution (reproduced in the top panel of Fig. 11) shows a moderate dependence on M_{UV}, with the UV-faint population containing a larger proportion of higher $\mathrm{REW}_{\mathrm{Ly}\alpha}$ galaxies. This is shown in an alternate way in the middle panel, which shows the cumulative distribution function (CDF) of these distributions. The CDF of the UV-bright population rises to unity quickly, representing a wealth of low-$\mathrm{REW}_{\mathrm{Ly}\alpha}$ galaxies. Since we only wish to examine galaxies with $\mathrm{REW}_{\mathrm{Ly}\alpha} > 25$ Å, we examine the $\mathrm{REW}_{\mathrm{Ly}\alpha}$ distribution as normalized by the 25 Å value (bottom panel of Fig. 11). These normalized distributions are quite similar, with differences of $\lesssim 10$ per cent. Based on this similarity across M_{UV} values, we adopt the $M_{\mathrm{UV}} = -18.5$ distribution when constructing our models.

To begin, we derive mean error spectra for each tier. For each observed galaxy, we create 30 high-resolution mock spectra using the R100-blue model from Section 3.1 with different realizations of the appropriate noise spectrum. Each model has the same M_{UV} and redshift as the observed galaxy, but with a variable $\mathrm{REW}_{\mathrm{Ly}\alpha}$ (sampled from the $\mathrm{REW}_{\mathrm{Ly}\alpha}$ distribution described previously, with limits of 25 Å $\leq \mathrm{REW}_{\mathrm{Ly}\alpha} \leq 500$ Å), β (sampled from a uniform distribution
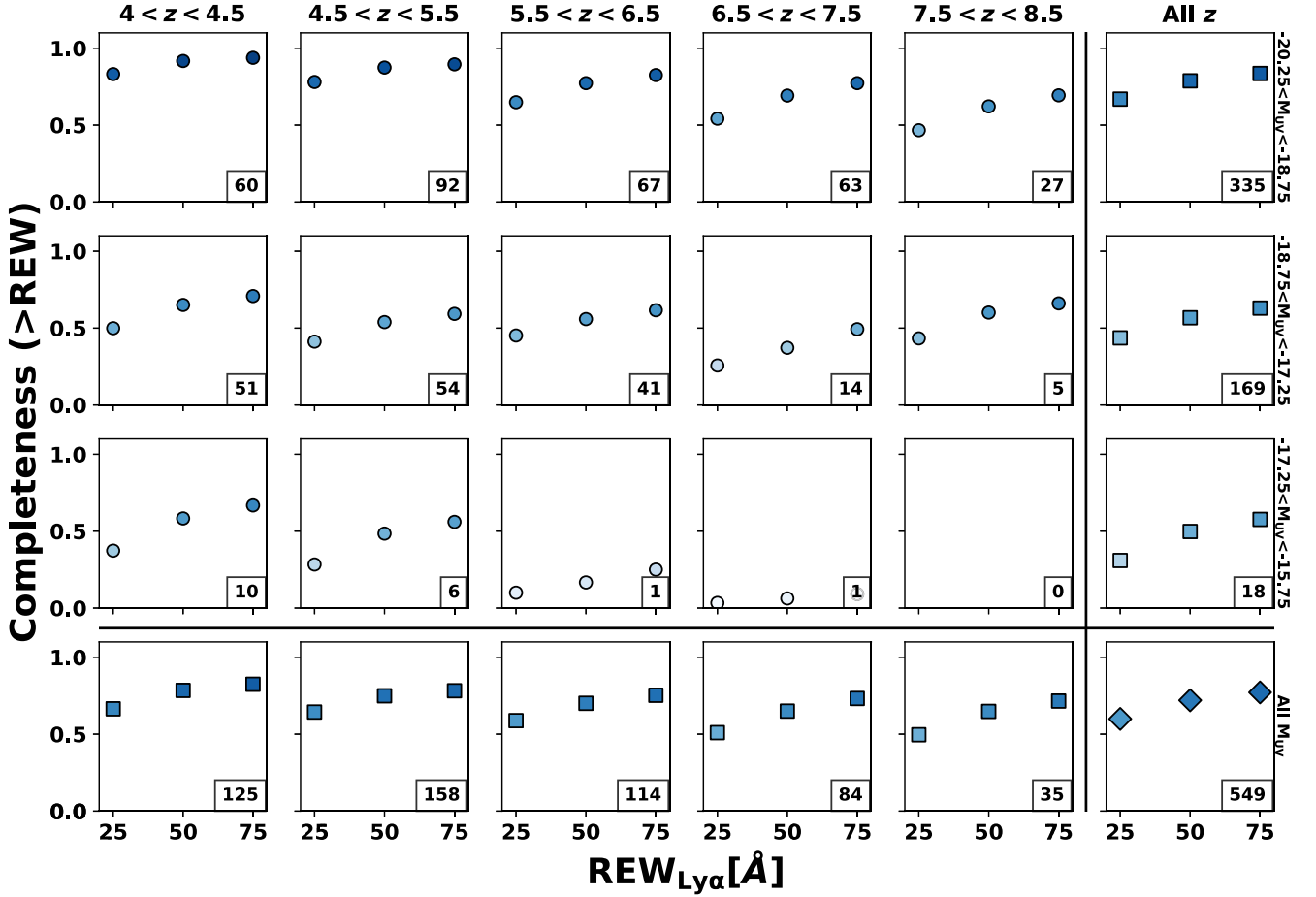
Figure 12. Completeness of galaxies in our sample for three $REW_{Ly\alpha}$ limits, divided into bins of redshift (columns, increasing from left to right) and M_{UV} (rows, decreasing in brightness from top to bottom). Darker points indicate higher completeness. The lower row and rightmost column show the completeness with no limits on M_{UV} and redshift, respectively. Thus, the lower right panel is the completeness of the full sample. The number of galaxies in each bin is shown the lower right of each panel.

between [−2.5, 2.5]),[10] and deviation from the fiducial LSF (F_R; sampled from a uniform distribution between [0.5, 1.0]). For this analysis, we exclude all galaxies from each tier whose M_{UV} value cannot be measured directly from the R100 data due to high noise levels, as their $REW_{Ly\alpha}$ is poorly constrained. Since we are able to constrain $REW_{Ly\alpha}$ across a wide range of M_{UV} values (Fig. 4), this does not strongly affect our analysis.

Each model is fit using the R100-blue model of Section 3.1, and we record the best-fitting $REW_{Ly\alpha}$ (REW_{obs}) and the associated uncertainty (δREW_{obs}). The completeness for an observed galaxy at the given $REW_{Ly\alpha}$ limit (hereafter $C_j(> REW_{lim})$) is derived by dividing the number of models that meet the $REW_{Ly\alpha}$ limit with successful Lyα detections ($REW_{obs} > 3\delta REW_{obs}$ and $< 3\sigma$ difference between REW_{obs} and REW_{input}) by the number of such simulations. As an example, consider the galaxy with ID 1655 in 1181_MHN ($z_{sys} = 4.474$), which yields $C_j(> 25\,\text{Å}) \sim 60$ per cent, $C_j(> 50\,\text{Å}) \sim 89$ per cent, and $C_j(> 75\,\text{Å}) \sim 93$ per cent.

This analysis allows us to examine the completeness of our sample and technique as a function of galaxy properties. We calculate the average completeness for our sample in bins of redshift and M_{UV}, excluding galaxies for which our completeness analysis returned

$C_j(> 25\,\text{Å}) = 0$. As shown in Fig. 12, the completeness increases with $REW_{Ly\alpha}$ for nearly all bins. The completeness decreases strongly with M_{UV}, with $C \lesssim 50$ per cent for the UV-faint bin. Since the majority of our sources lie in the $−20.25 < M_{UV} < −18.75$ bin, our average completeness is $\sim 50 − 80$ per cent.

5.2.2 Lyα fraction determination

The Lyα fraction for each redshift bin (z_i, e.g. $4.5 < z < 5.5$) and $REW_{Ly\alpha}$ bin (e.g. $REW_{lim} = 25$ Å) is then evaluated as:

$$X_{Ly\alpha}(z_i, REW > REW_{lim}) = \frac{N_{det}(> REW_{lim})}{\sum_j^{N_{obs}} C_j(> REW_{lim})}, \quad (11)$$

where $N_{det}(> REW_{lim})$ is the subset of these galaxies with a detected $REW_{Ly\alpha}$ greater than REW_{lim} and N_{obs} is the total number of observed galaxies that meet the z and M_{UV} requirements. Because the completeness factor is bound between zero and unity, this form of $X_{Ly\alpha}$ will always be equal to or greater than the form lacking a completeness correction. For this calculation, we exclude galaxies where M_{UV} was not measurable from the R100 spectra, as well as galaxies with $C_j(> REW_{lim}) = 0$.

The resulting evolution of Lyα fraction with redshift is shown in Fig. 13, along with values from literature (Stark et al. 2010;

---

[10]Note that this slope is different from β_{UV}, see Section 3.1.
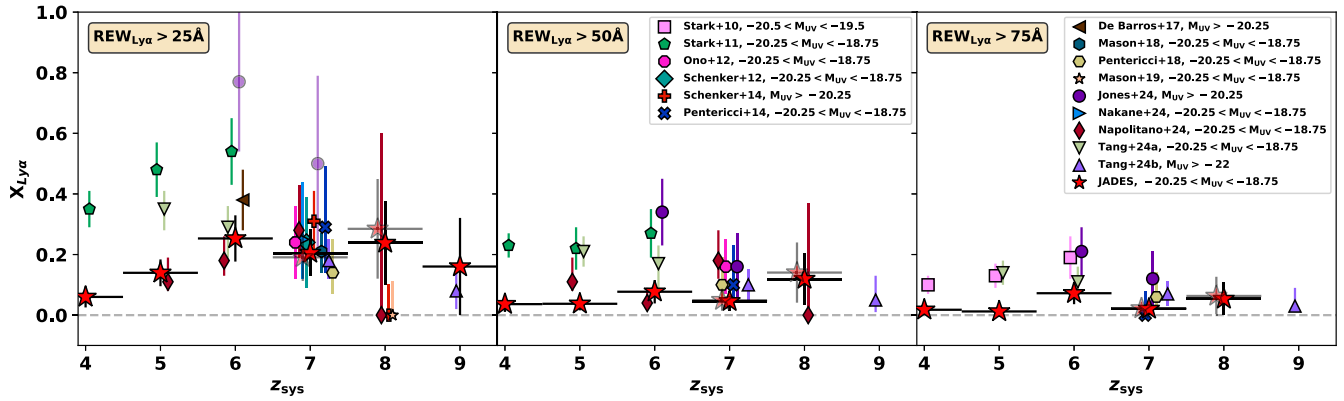
Figure 13. Fraction of observed galaxies detected in Lyα emission with $REW_{Ly\alpha} > 25\,\text{Å}$ (left), $REW_{Ly\alpha} > 50\,\text{Å}$ (centre), and $REW_{Ly\alpha} > 75\,\text{Å}$ (right). Our derived fractions are shown as red stars, while fractions from literature are shown by coloured markers (Stark et al. 2010; Stark et al. 2011; Ono et al. 2012; Schenker et al. 2012; Pentericci et al. 2014, 2018; Schenker et al. 2014; De Barros et al. 2017; Mason et al. 2018a, 2019; Jones et al. 2024; Nakane et al. 2024; Napolitano et al. 2024; Tang et al. 2024a, b). Points are shifted in redshift for clarity. The $REW_{Ly\alpha} > 25\,\text{Å}$ points of Jones et al. (2024) were affected by low completeness, so we display them with low opacity. For the central panel, note that Stark et al. (2011) and Ono et al. (2012) used a $REW_{Ly\alpha}$ limit of $> 55\,\text{Å}$. The Lyα fractions calculated by excluding the eight galaxies in possible galaxy overdensities (see Section 2.2) are depicted by low-opacity red stars.

Stark et al. 2011; Ono et al. 2012; Schenker et al. 2012; Pentericci et al. 2014; Schenker et al. 2014; De Barros et al. 2017; Mason et al. 2018a, 2019; Pentericci et al. 2018; Jones et al. 2024; Nakane et al. 2024; Napolitano et al. 2024; Tang et al. 2024a, b). For this comparison, we exclude some Lyα fractions derived only using UV-bright galaxies ($M_{UV} < -20.25$; Curtis-Lake et al. 2012; Cassata et al. 2015; Furusawa et al. 2016; Stark et al. 2017; Yoshioka et al. 2022; Fu et al. 2024), as these are found to have systematic differences (e.g. Stark et al. 2011; Pentericci et al. 2014, 2018). To avoid overcrowding of the figure, we also do not include all available studies (e.g. Mallery et al. 2012; Treu et al. 2013; Caruana et al. 2014; Tilvi et al. 2014; Fuller et al. 2020; Kusakabe et al. 2020; Goovaerts et al. 2023). The fractions for Tang et al. (2024a, b) are derived by integrating their best-fitting $REW_{Ly\alpha}$ distributions. We note that Napolitano et al. (2024) presents Lyα fractions derived using multiple data sets (i.e. JADES and CEERS). For each redshift bin, we include their result with the largest sample size with overdensity correction, if available.

For most data sets, there is a clear increase in $X_{Ly\alpha}$ from $z = 4$ to $z = 6$ and a decrease for $z > 6$, due presumably to enhanced IGM absorption. However, a clear spread in values is present for each redshift bin (likely due to changes in stellar populations and ISM properties). Our $X_{Ly\alpha}$ values for $4 < z < 6.5$ are lower than those of archival studies that used DEIMOS on Keck (i.e. Stark et al. 2010; Stark et al. 2011), but are comparable to other *JWST* studies (i.e. Napolitano et al. 2024; Tang et al. 2024a) as well as a study that used the FOcal Reducer/low dispersion Spectrograph 2 (FORS2) on the Very Large Telescope (VLT; De Barros et al. 2017).

As one of the first redshift bins containing galaxies in the EoR, the Lyα fraction at $6.5 < z < 7.5$ has been very well explored. Our fractions are in agreement with the other results. We previously found that some of the Lyα emitting galaxies in the $7.5 < z < 8.5$ bin may lie in galaxy overdensities (see Section 2.2). Since these may trace regions of increased Lyα transmission (e.g. Ouchi et al. 2010), we also estimate the Lyα fraction when these galaxies are excluded (see faint red stars in Fig. 13). This results in lower $X_{Ly\alpha}$ values, but not significantly (i.e. $< 1\sigma$). The highest redshift bin ($8.5 < z < 9.5$) has not yet been well explored, but our low fraction agrees with the findings of Tang et al. (2024b).

To summarize, our derived Lyα fractions imply a similar evolution as previous studies: an increase from early times ($z \sim 9.5$) to the end of the EoR (between $5.5 < z < 6.5$), followed by a decrease to $z \sim 4$. We briefly note that proper constraints on $X_{Ly\alpha}$ require knowledge of the effects of cosmic variance, selection effects, and observational biases. The JADES survey is well-suited to the discovery of LAEs, but due to its relatively small survey area (i.e. the GOODS fields) and the pre-selection of sources to be observed with the NIRSpec MSA, we may be affected by these effects. Future studies including more fields will correct this effect, but they must also take completeness into account.

5.3 Neutral hydrogen fraction

The evolution of the neutral hydrogen fraction is key to the study of the EoR, as it directly traces the process of reionization. A number of studies have constrained this evolution using different techniques, including DW modelling (e.g. Ďurovčíková et al. 2024; Spina et al. 2024; Umeda et al. 2024), detailed reionization simulations (e.g. Morales et al. 2021; Asthana et al. 2024; Bhagwat et al. 2024b; Mukherjee, Dey & Pal 2024), and analysis of Lyα fractions (e.g. Ono et al. 2012; Furusawa et al. 2016; Mason et al. 2018b; Jones et al. 2024). While a general evolution from $X_{HI} = 1$ at $z \gtrsim 9$ to $X_{HI} \sim 0$ at $z \sim 6$ is observed, the exact evolution of this fraction for $z \sim 6 - 9$ is not yet well constrained. Here, we combine our Lyα fractions with the model outputs of Dijkstra, Mesinger & Wyithe (2011) to place constraints on the neutral fraction at $z \sim 7$.

The model originally created in Dijkstra et al. (2011) was built on the assumption that the evolution of the Lyα fraction between $z = 7$ and $z = 6$ (a period of $\sim 170\,\text{Myr}$) is predominantly dictated by a changing neutral fraction (X_{HI}). While the intrinsic distribution of $REW_{Ly\alpha}$ may also evolve due to changes in galaxy population properties (e.g. metallicity, ISM conditions), the small time-scale between these redshifts makes this assumption reasonable. In addition, they assume that the $REW_{Ly\alpha}$ distribution at $z = 6$ may be described by an exponential with scale length $REW_{Ly\alpha,c} = 50\,\text{Å}$. Further studies using additional observations (e.g. Pentericci et al. 2018; Nakane et al. 2024) determined that $REW_{Ly\alpha,c}$ was lower ($\sim 30 - 40\,\text{Å}$).
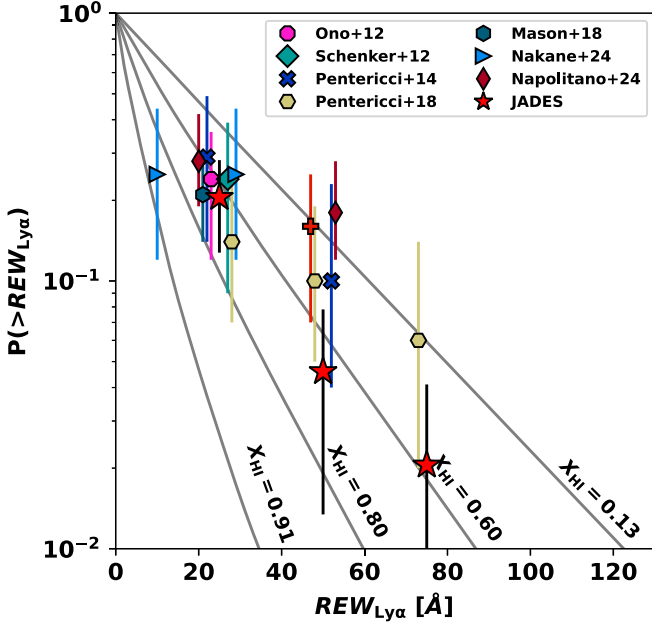
Figure 14. Cumulative distribution for REW$_{Ly\alpha}$ at $z \sim 7$ using galaxies with $-20.25 < M_{UV} < -18.75$. Each solid line shows the expected distribution for a model with $N_{HI} = 10^{20}\,\mathrm{cm}^{-2}$, a wind speed of $200\,\mathrm{km\,s}^{-1}$, and an assumed intrinsic REW$_{Ly\alpha}$ distribution scale length of 30 Å, but with a different neutral fraction (Nakane et al. 2024). Estimates from the literature (Ono et al. 2012; Schenker et al. 2012; Pentericci et al. 2014, 2018; Mason et al. 2018a; Nakane et al. 2024; Napolitano et al. 2024) are shifted by 1 Å for visibility.

This model was recently utilized by Nakane et al. (2024), who assumed $N_{HI} = 10^{20}\,\mathrm{cm}^{-2}$ and outflow speed $v_{wind} = 200\,\mathrm{km\,s}^{-1}$ and restricted the galaxy sample to those with $-20.25 < M_{UV} < -18.75$. As part of their results, they include a set of REW$_{Ly\alpha}$ distributions for different values of REW$_{Ly\alpha,c}$ and $X_{HI}(z = 7)$.

In order to investigate the neutral fraction at $z \sim 7$, we isolate all galaxies between $6.5 < z < 7.5$ and enforce the same M_{UV} cut as other works ($-20.25 < M_{UV} < -18.75$). Using the M_{UV}-dependent parametrization of Mason et al. (2018a),[11] this M_{UV} range corresponds to REW$_{Ly\alpha,c} \sim 31 - 32$ Å. We convert the REW$_{Ly\alpha}$ PDFs of Nakane et al. (2024) for REW$_{Ly\alpha,c} = 30$ Å to CDFs, and compare our completeness-corrected $X_{Ly\alpha}(z = 7)$ cumulative distribution with these model outputs and a set of literature values in Fig. 14. The values of our sample are in agreement (i.e. $\lesssim 2\sigma$ discrepancy) with the other values, as previously seen in Fig. 13.

Next, we estimate X_{HI} using the sets of measurements in Fig. 14. Each $X_{Ly\alpha}$ value and its uncertainties represents a probability distribution of $P(> \mathrm{REW}_{Ly\alpha,lim})$ for REW$_{Ly\alpha,lim} \in [25, 50, 75]$ Å, while the model grid of Nakane et al. (2024) may be used to convert $P(> \mathrm{REW}_{Ly\alpha,lim})$ into a distribution of X_{HI} for each REW$_{Ly\alpha,lim}$ value. The combination of these distributions for our data results in an estimate of $X_{HI} = 0.64^{+0.13}_{-0.21}$ for our $-20.25 < M_{UV} < -18.75$ sample. If we instead use the model outputs of Pentericci et al. (2014), which assumes REW$_{Ly\alpha,c} = 50$ Å, then we find a higher value ($X_{HI} = 0.89^{+0.04}_{-0.06}$; see Appendix E).

To put this result in context, we compare our best-fitting X_{HI} value to those of literature in Fig. 15. While there are a multitude of estimates that have been made over the last decades, there are a

[11]REW$_{Ly\alpha,c} = 31 + 12 \tanh[4(M_{UV} + 20.25)]$ Å

few illustrative boundaries. The first is composed of the conservative upper limits at $5.5 \lesssim z \lesssim 6.7$ based on studies of dark pixels in Lyα and Lyβ forests (e.g. McGreer et al. 2015; Jin et al. 2023), which constrain the end of the EoR. We may also consider the constraints of two different models (Finkelstein et al. 2019; Naidu et al. 2020). The former charts the progress of reionization if the budget of reionising photons is primarily supplied by UV-faint ($M_{UV} > -15$) galaxies, while reionisation in the latter model is dominated by UV-bright objects ($M_{UV} < -18$; 'oligarchs'). Regardless of the method used, most observations result in X_{HI} estimates that fall between these two models. Our value of $X_{HI}(z = 7) = 0.64^{+0.13}_{-0.21}$ is in agreement with those of other studies, which predict a value of ~ 0.5 at $z = 7$ (e.g. Mason et al. 2018a; Greig et al. 2022; Ďurovčíková et al. 2024; Nakane et al. 2024; Tang et al. 2024b).

6 CONCLUSIONS

Using the rich *JWST*/NIRSpec data set of the full JADES survey, we have searched for Lyα emission in a sample of 795 galaxies at $4.0 < z < 14.3$, resulting in the detection of 150 LAEs spanning the end of the EoR to nearly cosmic dawn ($4.0 < z < 13.1$). Due to the construction of the JADES survey, galaxies in our sample are distributed across the GOODS-N and GOODS-S fields, with LAEs detected over a wide range of M_{UV} (from -16 to -21).

The low-resolution R100 data allowed for estimates of the underlying continuum emission, while the wide wavelength coverage ($\lambda_{obs} = 0.6 - 5.3\,\mu\mathrm{m}$) permitted the detection of rest-optical lines (e.g. [O III]$\lambda\lambda$4959, 5007, Hα). Most galaxies also benefit from higher resolution R1000 data, which open a more detailed window into the fluxes of each line and the velocity offset of Lyα. The resulting line and continuum properties were analysed to characterize this unique sample of galaxies.

Similarly to previous works, our data show a positive relation between REW$_{Ly\alpha}$ and M_{UV} across a range of redshifts. While this correlation was proposed to be the result of sensitivity effects (i.e. a lack of galaxies with faint Lyα and continuum emission; Jones et al. 2024), we still find a strong correlation in each redshift bin using our large sample that includes deep observations. Thus, the correlation is likely physical.

We calculate the Lyα escape fraction of our sample using R1000 data and calculating the intrinsic Lyα flux using the observed Hβ flux (see Appendix C4 for discussion of this assumption). This value shows a strong positive correlation with REW$_{Ly\alpha}$ (in agreement with e.g. Roy et al. 2023). There is a strong negative correlation between $f_{esc}^{Ly\alpha}$ and redshift ($z \sim 5.5 - 9.5$), which may reflect IGM evolution during the EoR.

To explore the reionizing properties of individual galaxies, we examine the relation between Lyα velocity offset and $f_{esc}^{Ly\alpha}$, which shows a negative correlation. For galaxies in the EoR, Lyα near the systemic redshift will be absorbed or scattered from the line of sight, and only Lyα at high relative velocities will be able to escape. As the galaxies ionize their surroundings, a lower velocity offset is required. Thus, this negative correlation also represents a direct tracer of reionisation on the galaxy scale.

All REW$_{Ly\alpha}$ measurements (both detections and upper limits) are then combined with the Bayesian framework of Mason et al. (2018a) to constrain the IGM transmission of Lyα (T_{IGM}) between $z = 6 - 14$ as a function of $T_{IGM}(z \sim 5)$. We find a similar evolution as Tang et al. (2024b): a decrease of ~ 50 per cent between $z = 5 - 7$, and a further decrease of ~ 20 per cent between $z = 7 - 12$.

Using the observed properties of our galaxies, and a set of mock spectra, we determine the REW$_{Ly\alpha}$ completeness of our sample and
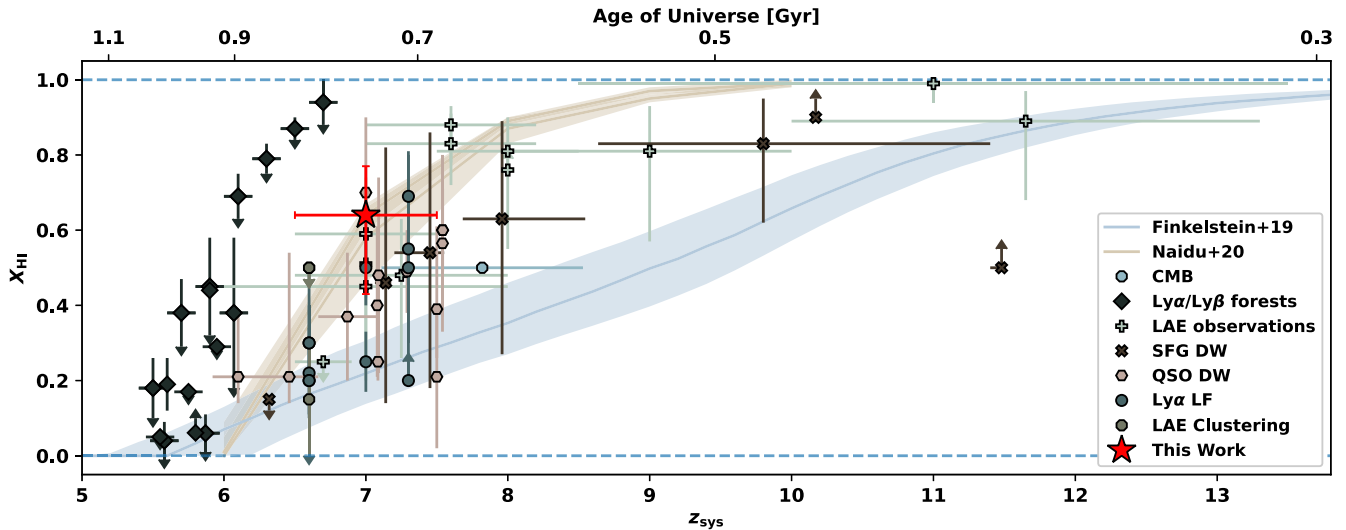
Figure 15. Comparison of X_{HI} values derived through diverse methods. Our value, as derived through a comparison of the observed $X_{Ly\alpha}$ distribution to the model grid of Pentericci et al. (2014), is shown as a large black star. We include the results of two reionization models (Finkelstein et al. 2019; Naidu et al. 2020), a detailed CMB study (Planck Collaboration VI 2020), $Ly\alpha$ and $Ly\beta$ forest observations (McGreer et al. 2015; Zhu et al. 2022; Jin et al. 2023; Spina et al. 2024; Zhu et al. 2024), LAE observations (Schenker et al. 2014; Mason et al. 2018a; Hoag et al. 2019; Mason et al. 2019; Bolan et al. 2022; Jones et al. 2024; Nakane et al. 2024; Tang et al. 2024b), $Ly\alpha$ damping wings of star forming galaxies (Curtis-Lake et al. 2023; Fausey et al. 2024; Hsiao et al. 2024; Umeda et al. 2024) and QSOs (Greig et al. 2017; Bañados et al. 2018; Davies et al. 2018; Greig, Mesinger & Bañados 2019; Ďurovčíková et al. 2020; Wang et al. 2020; Yang et al. 2020; Greig et al. 2022; Ďurovčíková et al. 2024), $Ly\alpha$ luminosity functions (Ouchi et al. 2010; Konno et al. 2014; Zheng et al. 2017; Inoue et al. 2018; Konno et al. 2018; Goto et al. 2021; Morales et al. 2021; Ning et al. 2022), and LAE clustering (Ouchi et al. 2010; Sobacchi & Mesinger 2015; Ouchi et al. 2018).

analysis technique. Instead of completeness at a given $REW_{Ly\alpha}$ value, we are interested instead in the completeness for all values above a $REW_{Ly\alpha}$ limit, and thus adopt a previously found $REW_{Ly\alpha}$ distribution (Tang et al. 2024a) in our derivation. This analysis reveals that our completeness increases from ~ 50 per cent for $REW_{Ly\alpha} > 25$ Å to ~ 70 per cent for $REW_{Ly\alpha} > 75$ Å across most redshift and M_{UV} bins. We strongly recommend implementing completeness analyses for future works investigating $Ly\alpha$ emission in large *JWST* data sets, as its exclusion introduces a non-trivial bias in the results.

A completeness correction is applied to the sample to create $Ly\alpha$ fraction distributions: $X_{Ly\alpha}(z)$. We find that $X_{Ly\alpha}$ increases between $z = 4 - 6$ and decreases at higher redshifts, in line with other works. A non-zero $X_{Ly\alpha}(z \sim 8)$ is found, which we verify is not biased by observing galaxy overdensities.

The $X_{Ly\alpha}(z = 7)$ values are combined with the model of Nakane et al. (2024) to place a constraint on $X_{HI}(z = 7) = 0.64^{+0.13}_{-0.21}$. Applying the same method to $Ly\alpha$ fractions from other works results in similar X_{HI} values. This is placed in context with other $X_{HI}(z \sim 5.3 - 13.5)$ values, where it is made clear that our hydrogen neutral fraction is comparable to most values derived in other works.

By exploiting the large data set of JADES, we have unveiled a number of new LAEs spanning a wide range of intrinsic properties and cosmic epochs. Ongoing and future investigations will detail individual LAEs, and this sample will be combined with other large surveys to shine light on the remaining mysteries of the EoR.

DATA AVAILABILITY

The data underlying this article will be shared on reasonable request to the corresponding author.

REFERENCES

Asthana S., Haehnelt M. G., Kulkarni G., Aubert D., Bolton J. S., Keating L. C., 2024, MNRAS, 533, 2843
Austin D. et al., 2024, preprint (arXiv:2404.10751)
Bañados E. et al., 2018, Nature, 553, 473
Becker G. D., Bolton J. S., Zhu Y., Hashemi S., 2024, MNRAS, 533, 1525

Beckwith S. V. W. et al., 2006, AJ, 132, 1729
Begley R. et al., 2024, MNRAS, 527, 4040
Bhagwat A., Costa T., Ciardi B., Pakmor R., Garaldi E., 2024b, MNRAS, 531, 3406
Bhagwat A., Napolitano L., Pentericci L., Ciardi B., Costa T., 2024a, preprint (arXiv:2408.16063)
Bhatawdekar R., Conselice C. J., 2021, ApJ, 909, 144
Binggeli C. et al., 2019, MNRAS, 489, 3827
Böker T. et al., 2023, PASP, 135, 038001
Bolan P. et al., 2022, MNRAS, 517, 3263
Bonaventura N., Jakobsen P., Ferruit P., Arribas S., Giardino G., 2023, A&A, 672, A40
Bosman S. E. I. et al., 2022, MNRAS, 514, 55
Bruzual G., Charlot S., 2003, MNRAS, 344, 1000
Bunker A. J. et al., 2023, A&A, 677, A88
Bunker A. J. et al., 2024, A&A, 690, A288
Bunker A. J., NIRSPEC Instrument Science Team, JAESs Collaboration, 2020, in da Cunha E., Hodge J., Afonso J., Pentericci L., Sobral D., eds, Proc. IAU Symp. 352, Uncovering Early Galaxy Evolution in the ALMA and JWST Era. Cambridge Univ. Press, Cambridge, p. 342
Calzetti D., Armus L., Bohlin R. C., Kinney A. L., Koornneef J., Storchi-Bergmann T., 2000, ApJ, 533, 682
Calzetti D., Kinney A. L., Storchi-Bergmann T., 1994, ApJ, 429, 582
Cameron A. J., Katz H., Witten C., Saxena A., Laporte N., Bunker A. J., 2024, MNRAS, 534, 523
Carniani S. et al., 2024, Nature, 633, 318
Caruana J., Bunker A. J., Wilkins S. M., Stanway E. R., Lorenzoni S., Jarvis M. J., Ebert H., 2014, MNRAS, 443, 2831
Cassata P. et al., 2015, A&A, 573, A24
Cassata P. et al., 2020, A&A, 643, A6
Chisholm J. et al., 2018, A&A, 616, A30
Chisholm J. et al., 2022, MNRAS, 517, 5104
Choustikov N. et al., 2024, MNRAS, 532, 2463
Cuby J. G., Le Fèvre O., McCracken H., Cuillandre J. C., Magnier E., Meneux B., 2003, A&A, 405, L19
Cullen F. et al., 2023, MNRAS, 520, 14
Curti M. et al., 2024a, preprint (arXiv:2407.02575)
Curti M. et al., 2024b, A&A, 684, A75
Curtis-Lake E. et al., 2012, MNRAS, 422, 1425
Curtis-Lake E. et al., 2023, Nat. Astron., 7, 622
D'Eugenio F. et al., 2024, preprint (arXiv:2404.06531)
Davies F. B. et al., 2018, ApJ, 864, 142
De Barros S. et al., 2017, A&A, 608, A123
de Graaff A. et al., 2024, A&A, 684, A87
Dickinson M., Giavalisco M., GOODS Team, 2003, in Bender R., Renzini A., eds, The Mass of Galaxies at Low and High Redshift. Springer, Berlin, p. 324
Dijkstra M., 2009, ApJ, 690, 82
Dijkstra M., Mesinger A., Wyithe J. S. B., 2011, MNRAS, 414, 2139
Domínguez A. et al., 2013, ApJ, 763, 145
Donnan C. T. et al., 2023, MNRAS, 518, 6011
Duan Q. et al., 2024, preprint (arXiv:2407.09472)
Ďurovčíková D. et al., 2024, ApJ, 969, 162
Ďurovčíková D., Katz H., Bosman S. E. I., Davies F. B., Devriendt J., Slyz A., 2020, MNRAS, 493, 4256
Eisenstein D. J. et al., 2023a, preprint (arXiv:2306.02465)
Eisenstein D. J. et al., 2023b, preprint (arXiv:2310.12340)
Eldridge J. J., Stanway E. R., 2012, MNRAS, 419, 479
Endsley R. et al., 2022, MNRAS, 517, 5642
Endsley R., Behroozi P., Stark D. P., Williams C. C., Robertson B. E., Rieke M., Gottlöber S., Yepes G., 2020, MNRAS, 493, 1178
Fan X. et al., 2006, AJ, 132, 117
Fausey H. M. et al., 2024, preprint (arXiv:2403.13126)
Feldmann R. et al., 2024, preprint (arXiv:2407.02674)
Ferruit P. et al., 2022, A&A, 661, A81
Finkelstein S. L. et al., 2019, ApJ, 879, 36
Fu S., Jiang L., Ning Y., Liu W., Pan Z., 2024, ApJ, 963, 51
Fujimoto S. et al., 2023, preprint (arXiv:2308.11609)
Fuller S. et al., 2020, ApJ, 896, 156

Furtak L. J. et al., 2024, MNRAS, 527, L7
Furusawa H. et al., 2016, ApJ, 822, 46
Gardner J. P. et al., 2023, PASP, 135, 068001
Goovaerts I. et al., 2023, A&A, 678, A174
Gordon K. D., Clayton G. C., Misselt K. A., Landolt A. U., Wolff M. J., 2003, ApJ, 594, 279
Goto H. et al., 2021, ApJ, 923, 229
Grazian A. et al., 2024, ApJ, 974, 84
Greig B., Mesinger A., Bañados E., 2019, MNRAS, 484, 5094
Greig B., Mesinger A., Davies F. B., Wang F., Yang J., Hennawi J. F., 2022, MNRAS, 512, 5390
Greig B., Mesinger A., Haiman Z., Simcoe R. A., 2017, MNRAS, 466, 4239
Grogin N. A. et al., 2011, ApJS, 197, 35
Gupta A. et al., 2023, ApJ, 957, L35
Hainline K. N. et al., 2024, ApJ, 976, 160
Hall P. B. et al., 2004, AJ, 127, 3146
Harikane Y. et al., 2023, ApJS, 265, 5
Hassan S., Davé R., Mitra S., Finlator K., Ciardi B., Santos M. G., 2018, MNRAS, 473, 227
Hausen R., Robertson B. E., 2022, Astron. Comput., 39, 100586
Heintz K. E. et al., 2024a, preprint (arXiv:2404.02211)
Heintz K. E. et al., 2024b, Science, 384, 890
Helton J. M. et al., 2024, ApJ, 974, 41
Hoag A. et al., 2019, ApJ, 878, 12
Hsiao T. Y.-Y. et al., 2024, ApJ, 973, 8
Inoue A. K. et al., 2018, PASJ, 70, 55
Izotov Y. I., Schaerer D., Guseva N. G., Thuan T. X., Worseck G., 2024, MNRAS, 528, L10
Jakobsen P. et al., 2022, A&A, 661, A80
Jiang H. et al., 2024, ApJ, 972, 121
Jin X. et al., 2023, ApJ, 942, 59
Johnstone R. M., Canning R. E. A., Fabian A. C., Ferland G. J., Lykins M., Porter R. L., van Hoof P. A. M., Williams R. J. R., 2012, MNRAS, 425, 1421
Jones G. C. et al., 2024, A&A, 683, A238
Jung I. et al., 2022, preprint (arXiv:2212.09850)
Jung I. et al., 2024, ApJ, 967, 73
Katz H. et al., 2024, preprint (arXiv:2408.03189)
Keating L. C., Kulkarni G., Haehnelt M. G., Chardin J., Aubert D., 2020b, MNRAS, 497, 906
Keating L. C., Weinberger L. H., Kulkarni G., Haehnelt M. G., Chardin J., Aubert D., 2020a, MNRAS, 491, 1736
Kerutt J. et al., 2022, A&A, 659, A183
Klessen R. S., Glover S. C. O., 2023, ARA&A, 61, 65
Konno A. et al., 2014, ApJ, 797, 16
Konno A. et al., 2018, PASJ, 70, S16
Kulkarni G., Keating L. C., Haehnelt M. G., Bosman S. E. I., Puchwein E., Chardin J., Aubert D., 2019, MNRAS, 485, L24
Kumari N. et al., 2024, preprint (arXiv:2406.11997)
Kusakabe H. et al., 2020, A&A, 638, A12
Langeroodi D., Hjorth J., 2024, preprint (arXiv:2404.13045)
Laseter I. H. et al., 2024, A&A, 681, A70
Li Y., Leja J., Johnson B. D., Tacchella S., Naidu R. P., 2024, ApJ, 969, L5
Luridiana V., Morisset C., Shaw R. A., 2015, A&A, 573, A42
Madau P., Giallongo E., Grazian A., Haardt F., 2024, ApJ, 971, 75
Mallery R. P. et al., 2012, ApJ, 760, 128
Mason C. A. et al., 2018b, ApJ, 857, L11
Mason C. A. et al., 2019, MNRAS, 485, 3947
Mason C. A., Treu T., Dijkstra M., Mesinger A., Trenti M., Pentericci L., de Barros S., Vanzella E., 2018a, ApJ, 856, 2
Matthee J., Mackenzie R., Simcoe R. A., Kashino D., Lilly S. J., Bordoloi R., Eilers A.-C., 2023, ApJ, 950, 67
McGreer I. D., Mesinger A., D'Odorico V., 2015, MNRAS, 447, 499
Meurer G. R., Heckman T. M., Calzetti D., 1999, ApJ, 521, 64
Morales A. M., Mason C. A., Bruton S., Gronke M., Haardt F., Scarlata C., 2021, ApJ, 919, 120
Mortlock D. J. et al., 2011, Nature, 474, 616
Mukherjee P., Dey A., Pal S., 2024, preprint (arXiv:2407.19481)

Naidu R. P., Tacchella S., Mason C. A., Bose S., Oesch P. A., Conroy C., 2020, ApJ, 892, 109

Nakane M. et al., 2024, ApJ, 967, 28

Napolitano L. et al., 2024, A&A, 688, A106

Narayanan D. et al., 2024, preprint (arXiv:2408.13312)

Navarro-Carrera R., Caputi K. I., Iani E., Rinaldi P., Kokorev V., Kerutt J., 2024, preprint (arXiv:2407.14201)

Newville M., Stensitzki T., Allen D. B., Ingargiola A., 2014, LMFIT: Non-Linear Least-Square Minimization and Curve-Fitting for Python. Zenodo. Available at: https://doi.org/10.5281/zenodo.11813

Ning Y., Jiang L., Zheng Z.-Y., Wu J., 2022, ApJ, 926, 230

Oesch P. A. et al., 2015, ApJ, 804, L30

Ono Y. et al., 2012, ApJ, 744, 83

Ouchi M. et al., 2010, ApJ, 723, 869

Ouchi M. et al., 2018, PASJ, 70, S13

Pentericci L. et al., 2014, ApJ, 793, 113

Pentericci L. et al., 2018, A&A, 619, A147

Planck Collaboration VI 2020, A&A, 641, A6

Planck Collaboration XIII 2016, A&A, 596, A108

Reddy N. A. et al., 2015, ApJ, 806, 259

Reddy N. A. et al., 2018, ApJ, 853, 56

Reddy N. A. et al., 2020, ApJ, 902, 123

Rieke M. J. et al., 2023, PASP, 135, 028001

Roberts-Borsani G. et al., 2024, ApJ, 976, 193

Robertson B. et al., 2024, ApJ, 970, 31

Roy N. et al., 2023, ApJ, 952, L14

Salim S., Boquien M., Lee J. C., 2018, ApJ, 859, 11

Saxena A. et al., 2023, A&A, 678, A68

Saxena A. et al., 2024a, A&A, 684, A84

Saxena A. et al., 2024b, preprint (arXiv:2411.14532)

Schenker M. A., Ellis R. S., Konidaris N. P., Stark D. P., 2014, ApJ, 795, 20

Schenker M. A., Stark D. P., Ellis R. S., Robertson B. E., Dunlop J. S., McLure R. J., Kneib J.-P., Richard J., 2012, ApJ, 744, 179

Seager S., Sasselov D. D., Scott D., 2000, ApJS, 128, 407

Shibuya T. et al., 2014, ApJ, 788, 74

Shibuya T. et al., 2018, PASJ, 70, S15

Sobacchi E., Mesinger A., 2015, MNRAS, 453, 1843

Sobral D., Matthee J., 2019, A&A, 623, A157

Song M., Finkelstein S. L., Livermore R. C., Capak P. L., Dickinson M., Fontana A., 2016, ApJ, 826, 113

Spina B., Bosman S. E. I., Davies F. B., Gaikwad P., Zhu Y., 2024, A&A, 688, L26

Stanway E. R., Bunker A. J., McMahon R. G., 2003, MNRAS, 342, 439

Stanway E. R., Bunker A. J., McMahon R. G., Ellis R. S., Treu T., McCarthy P. J., 2004, ApJ, 607, 704

Stanway E. R., Eldridge J. J., Becker G. D., 2016, MNRAS, 456, 485

Stark D. P. et al., 2017, MNRAS, 464, 469

Stark D. P., Ellis R. S., Chiu K., Ouchi M., Bunker A., 2010, MNRAS, 408, 1628

Stark D. P., Ellis R. S., Ouchi M., 2011, ApJ, 728, L2

Sunyaev R. A., Zeldovich I. B., 1980, ARA&A, 18, 537

Tacchella S. et al., 2024, preprint (arXiv:2404.02194)

Tang M. et al., 2023, MNRAS, 526, 1657

Tang M. et al., 2024a, MNRAS, 531, 2701

Tang M., Stark D. P., Topping M. W., Mason C., Ellis R. S., 2024b, ApJ, 975, 208

Terp C., Heintz K. E., Watson D., Brammer G., Carnall A., Witstok J., Smit R., Vejlgaard S., 2024, A&A, 690, A70

Tilvi V. et al., 2014, ApJ, 794, 5

Tilvi V. et al., 2020, ApJ, 891, L10

Topping M. W. et al., 2024, MNRAS, 529, 4087

Torralba-Torregrosa A. et al., 2024, A&A, 689, A44

Treu T., Schmidt K. B., Trenti M., Bradley L. D., Stiavelli M., 2013, ApJ, 775, L29

Umeda H., Ouchi M., Nakajima K., Harikane Y., Ono Y., Xu Y., Isobe Y., Zhang Y., 2024, ApJ, 971, 124

Vanzella E. et al., 2011, ApJ, 730, L35

Ventou E. et al., 2017, A&A, 608, A9

Virtanen P. et al., 2020, Nat. Methods, 17, 261

Wang F. et al., 2020, ApJ, 896, 23

Willott C. J. et al., 2013, AJ, 145, 4

Witstok J. et al., 2024a, preprint (arXiv:2408.16608)

Witstok J. et al., 2024b, A&A, 682, A40

Witstok J. et al., 2025, MNRAS, 536, 27

Witten C. E. C., Laporte N., Katz H., 2023, ApJ, 944, 61

Witten C. et al., 2024, Nat. Astron., 8, 384

Yamanaka S., Yamada T., 2019, PASJ, 71, 51

Yang J. et al., 2020, ApJ, 897, L14

Yoshioka T. et al., 2022, ApJ, 927, 32

Zheng Z.-Y. et al., 2017, ApJ, 842, L22

Zhu Y. et al., 2022, ApJ, 932, 76

Zhu Y. et al., 2024, MNRAS, 533, L49

APPENDIX A: M_{UV} LIMIT DISTRIBUTION

Throughout this work, the rest-UV magnitude M_{UV} is estimated directly from our *JWST*/NIRSpec R100 spectra. While these data are sensitive to the strength and shape of the rest-UV continuum (e.g. Topping et al. 2024), our sample features two types of diversity that hinder M_{UV} measurement: intrinsic UV brightness and observation depth. As seen in Fig. 5, our measured M_{UV} values extend over a range of $\delta M_{UV} \sim 5$ magnitudes, including both UV-luminous and faint galaxies (e.g. Stark et al. 2017). In addition, the JADES data set may be separated into a deep and medium tier (see Table 1), with a ~ 1 magnitude difference in sensitivity between the deepest and shallowest observations.

With this sample properties in mind, we consider the possibility that our M_{UV} measurement technique introduces a bias towards UV-bright galaxies. The distribution of our M_{UV} values (separated into measurements and upper limits) as a function of systemic redshift is shown in Fig. A1. It is clear that majority of the galaxies have reliable M_{UV} estimates (~ 85 per cent of the sample). Most of the upper limits are fainter than $M_{UV} = -18.75$, but we are able to measure M_{UV} for some galaxies below this threshold. This demonstrates that for the primary M_{UV} range of interest ($-20.25 < M_{UV} < -18.75$), we are able to measure M_{UV} well for most of our galaxies.

APPENDIX C: FIT QUALITY VERIFICATION

C1 R100–R1000 comparison

Because the R100 and R1000 fits were performed separately, we may directly compare the best-fitting integrated line flux for multiple strong emission lines (Fig. C1). For [O III]λ4959 and Hβ, the R1000-based fluxes are ~ 10 per cent larger. This agrees with the findings of Bunker et al. (2024), who used NIRCam comparisons to suggest that the R100-based fluxes may be more accurate.

In a curious reversal, we find that the R100-based estimates of [N II]λ6548 flux (of which there are not many 3σ detections) are lower than the R1000-based estimates. When comparing the R100- and R1000-based fluxes for Hα alone, excellent agreement (< 1 per cent deviation) is found. However, when the combined [N II]–Hα flux of the R1000 fit is compared to the Hα flux of the R100 fit, we find a similar ~ 14 per cent deviation in slope as in the other strong lines. This suggests that [N II]λ6548 and [N II]λ6584 are blended with Hα in the R100 spectra, and our R100-based Hα flux encompasses the full [N II]–Hα complex.
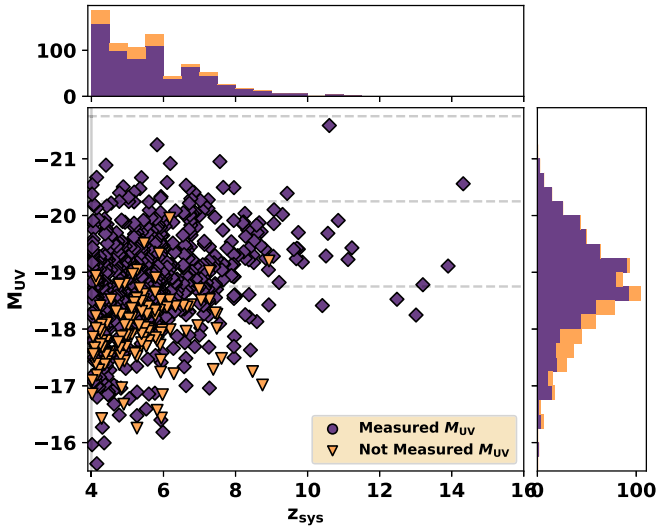
Figure A1. M_{UV} (from NIRSpec R100 spectra) versus systemic redshift (based on rest-frame optical lines) for our sample. Sources where M_{UV} is robustly measured from the observed R100 spectrum are shown by purple diamonds, while sources where M_{UV} is not well determined are shown by orange triangles.

The upper right panel of Fig. C1 instead presents the difference in spectroscopic redshift as derived from the R100 and R1000 spectra. We find a best-fitting offset of $\Delta z \sim 0.005$, which is consistent with the median offset presented by Bunker et al. (2024; 0.00388) and D'Eugenio et al. (2024; 0.0042). Thus, while the R100 and R1000 results are in approximate agreement, the disagreements in flux and wavelength suggest that they should be analysed separately.

C2 Grating redshift reliability

For each galaxy, we perform up to four separate fits: the full R100 spectrum, the R1000 data around Lyα, the R1000 data around the [O III]$\lambda\lambda 4959$, 5007–Hβ complex, and the R1000 data around the Hα–[N II]$\lambda\lambda 6548$, 6584 complex. These fits reveal that the resulting line fluxes and redshifts are in agreement (with the exception of calibration-level offsets, see Section C1).

However, it is also possible that the results from each of the three R1000 gratings may yield different results. To inspect this, we consider the redshifts derived from the [O III]$\lambda\lambda 4959$, 5007–Hβ complex (G235M) and the Hα–[N II]$\lambda\lambda 6548$, 6584 complex (G395M). As shown in Fig. C2, these redshifts are in great agreement, with an average deviation of only $|\delta z| = 0.00005$, or $< 5\,\mathrm{km\,s^{-1}}$. Thus, we do not find significant differences in redshifts from different R1000 gratings.

C3 Lyα velocity offset measurement

As discussed in Section 3.2, we measure the velocity offset of Lyα with respect to the redshift of the rest-optical lines in two ways: the centroid wavelength of a best-fitting Gaussian model ($\Delta v_{\mathrm{Ly}\alpha,\mathrm{G}}$) and the brightest pixel within $[-500, 1000]\,\mathrm{km\,s^{-1}}$ of Lyα ($\Delta v_{\mathrm{Ly}\alpha,\mathrm{P}}$). In Fig. C3, we show the difference between these velocities as a function of $\Delta v_{\mathrm{Ly}\alpha,\mathrm{P}}$.

Ideally, these two velocities would always agree, resulting in a line of slope 0. But we find that $\Delta v_{\mathrm{Ly}\alpha,\mathrm{G}} > \Delta v_{\mathrm{Ly}\alpha,\mathrm{P}}$ for the bulk of the galaxies. This is expected from simulations of how Lyα emission profiles are affected by IGM absorption (e.g. Mason et al. 2018a). Lyα is intrinsically shifted to the red, and the blue edge is preferably

absorbed, resulting in red wings. A symmetric Gaussian fit to these profiles returns a more positive centroid velocity than the peak-finding approach, and this difference correlates with asymmetry. Because lines with lower Δv have more absorption and feature higher asymmetry, it is expected that $\Delta v_{\mathrm{Ly}\alpha,\mathrm{G}} > \Delta v_{\mathrm{Ly}\alpha,\mathrm{P}}$ for sources with low $\Delta v_{\mathrm{Ly}\alpha,\mathrm{P}}$, and that this difference decreases with increasing $\Delta v_{\mathrm{Ly}\alpha,\mathrm{P}}$. This is what we observe.

C4 Lyα escape fraction calculation

By fitting the R100 and R1000 spectra, we have up to two estimates of the fluxes of Lyα, Hα, and Hβ (i.e. from the R100 and R1000 fits), as well as a single estimate of the flux of the continuum underlying the Lyα line (i.e. from the R100 fit). These may be used to determine two estimates of $\mathrm{REW}_{\mathrm{Ly}\alpha}$: $\mathrm{REW}_{\mathrm{Ly}\alpha,\mathrm{R100}}$ and $\mathrm{REW}_{\mathrm{Ly}\alpha,\mathrm{R1000}}$, where both use the same R100-based continuum value. In addition, we may calculate eight versions of $f_{\mathrm{esc}}^{\mathrm{Ly}\alpha}$: using the Lyα/H$\alpha$ or Lyα/Hβ ratio (see Section 3.2), including a dust correction based on the measured $E(B-V)$ or not (denoted DC or No_DC, respectively), and using values from the R100 or R1000 fits.

To examine these quantities further, we isolate a subsample of galaxies with both measures of $\mathrm{REW}_{\mathrm{Ly}\alpha}$ and all eight measures of $f_{\mathrm{esc}}^{\mathrm{Ly}\alpha}$ (i.e. detections of Lyα, Hα, and Hβ in R100 and R1000) and plot $f_{\mathrm{esc}}^{\mathrm{Ly}\alpha}$ as a function of $\mathrm{REW}_{\mathrm{Ly}\alpha}$ in Fig. C4. This comparison immediately yields several useful findings. First, the application of a dust correction (which is assumed to be identical for the Balmer lines and Lyα) shifts some escape fractions to high values. Some of these fractions are shifted to non-physical values of >100 per cent, suggesting that an incorrect dust correction was applied. Some studies have found that Lyα and Hα are extincted differently due to the resonant nature of Lyα (e.g. Roy et al. 2023; Begley et al. 2024; Choustikov et al. 2024), implying that different corrections are needed. This may also be an effect of our assumptions of case B recombination rather than case A, or our use of the Calzetti et al. (2000) law rather than others (e.g. Salim, Boquien & Lee 2018; Reddy et al. 2020).

The most crucial finding here is that all four non-dust corrected escape fractions show the same positive correlation. Throughout the analysis of the main text we consider the $f_{\mathrm{esc}}^{\mathrm{Ly}\alpha}$ value derived from the R1000 data using the Lyα/Hβ ratio with no dust correction, and the associated R1000-based $\mathrm{REW}_{\mathrm{Ly}\alpha}$. This is driven by our ability to detect Hβ in our data out to higher redshifts, uncertainty in the applicability of our applied dust correction, and the higher spectral resolution of the R1000 data.

APPENDIX D: FITSMAP EXTRACT

APPENDIX E: ALTERNATE X_{HI} ESTIMATE

In Section 5.3, we combined our observed $\mathrm{REW}_{\mathrm{Ly}\alpha}$ distribution at $6.5 < z < 7.5$ with the model outputs presented by Nakane et al. (2024) to place an estimate on $X_{HI}(z \sim 7)$. This model was chosen for its assumption of a physically motivated intrinsic $\mathrm{REW}_{\mathrm{Ly}\alpha}$ distribution with $\mathrm{REW}_{\mathrm{Ly}\alpha,\mathrm{c}} = 30\,\text{Å}$. Here, we demonstrate that the use of a model with a more top-heavy $\mathrm{REW}_{\mathrm{Ly}\alpha}$ distribution results in a higher estimated $X_{HI}(z \sim 7)$.

In Fig. E1, we plot our $\mathrm{REW}_{\mathrm{Ly}\alpha}$ CDF at $z \sim 7$, but include the model grid of Pentericci et al. (2014). This model is nearly identical to that of Nakane et al. (2024), but features an intrinsic $\mathrm{REW}_{\mathrm{Ly}\alpha}$ distribution with $\mathrm{REW}_{\mathrm{Ly}\alpha,\mathrm{c}} = 50\,\text{Å}$. This yields a best-fitting $X_{HI} =$

APPENDIX B: BEST-FITTING LYα PROPERTIES

Table B1. Best-fitting properties of JADES LAEs. For each, we list the NIRSpec ID, position, observational tier, visual inspection redshift (D'Eugenio et al. 2024), M_{UV} values measured from R100 spectra, and Lyα properties (REW$_{Lyα}$ and escape fraction) from the R100 and R1000 spectra. While all galaxies with significantly detected (i.e. $> 3\sigma$) Lyα are listed, the low continuum detections of some sources result in $< 3\sigma$ REW$_{Lyα}$ values. Upper limits are given as 3σ. Lyα equivalent widths are calculated using the best-fitting continuum value from the R100 data, while the escape fractions are calculated using the intrinsic Lyα/Hβ ratio with no dust correction. We present the truncated table here for illustration, but the full table (including additional line and continuum properties) is available upon request.

ID JADES-	z_{sys}	Tier	M_{UV}	$S_C(\lambda_{Lyα,obs})$ 10^{-21} erg s^{-1} cm^{-2} Å^{-1}	$F_{Lyα,R100}$ 10^{-20} erg s^{-1} cm^{-2}	REW$_{Lyα,R100}$ Å	$F_{Lyα,R1000}$ 10^{-20} erg s^{-1} cm^{-2}	REW$_{Lyα,R1000}$ Å
GS+53.06475−27.89024	13.0100	DJS_1287	−18.25 ± 0.23	< 0.23	44 ± 6	< 192	< 64	< 184
GN+189.10604+62.24204	10.6030	MJN_1181	−21.59 ± 0.03	21.73 ± 0.55	< 162	< 6	171 ± 39	7 ± 2
GS+53.15862−27.83408	8.8365	MJS_1286	−19.25 ± 0.23	4.11 ± 0.92	< 251	< 62	155 ± 28	38 ± 11
GS+53.10900−27.90084	8.7110	DJS_1287	−19.72 ± 0.04	6.26 ± 0.21	171 ± 16	28 ± 3	153 ± 28	25 ± 5
GS+53.15891−27.76508	8.4861	DJS_3215	−19.30 ± 0.05	5.11 ± 0.30	94 ± 22	19 ± 5	86 ± 14	18 ± 3
GN+189.19774+62.25696	8.2790	MHN_1181	−19.63 ± 0.09	6.59 ± 0.78	918 ± 60	150 ± 21	698 ± 55	115 ± 16
GS+53.13675−27.83746	8.2252	MJS_1286	−19.36 ± 0.15	2.77 ± 0.79	228 ± 56	< 105	145 ± 39	< 67
GS+53.08932−27.87270	8.2242	MJS_1286	−19.83 ± 0.09	4.81 ± 0.75	222 ± 55	50 ± 15	< 107	< 31
GS+53.07581−27.87938	8.1968	MJS_1286	−19.87 ± 0.09	12.70 ± 1.14	< 228	< 20	217 ± 36	19 ± 4
GS+53.15682−27.76716	7.9799	DHS_1210	−18.60 ± 0.07	3.11 ± 0.21	65 ± 16	23 ± 6	80 ± 19	29 ± 7
GS+53.07670−27.88957	7.9690	DJS_1287	−17.87 ± 0.21	< 0.83	< 113	< 242	66 ± 21	< 150
GS+53.11991−27.90158	7.9561	DJS_1287	−18.54 ± 0.10	3.54 ± 0.26	108 ± 14	34 ± 5	< 61	< 5
GS+53.10561−27.89186	7.9548	DJS_1287	−17.70 ± 0.20	2.25 ± 0.32	222 ± 15	108 ± 18	< 130	< 71
GS+53.09943−27.88038	7.9508	MJS_1286	−19.91 ± 0.07	11.72 ± 0.91	257 ± 55	25 ± 6	199 ± 34	19 ± 4
GS+53.11378−27.86238	7.9451	DJS_1287	−18.92 ± 0.07	5.21 ± 0.35	266 ± 18	57 ± 5	< 59	< 13
GS+53.05373−27.87789	7.8906	MJS_1286	−19.12 ± 0.18	5.57 ± 0.93	< 285	< 69	97 ± 29	< 20
GS+53.06029−27.86354	7.8854	MJS_1286	−18.94 ± 0.13	5.10 ± 0.59	< 185	< 44	79 ± 19	18 ± 5
GS+53.13347−27.76037	7.6590	MHS_1180	−20.50 ± 0.03	22.73 ± 0.86	352 ± 66	18 ± 3	177 ± 24	9 ± 1
GS+53.20042−27.78210	7.4809	MJS_1180	−19.23 ± 0.14	8.83 ± 1.20	< 230	< 36	257 ± 68	35 ± 10
GS+53.10105−27.87581	7.4729	MJS_1286	−18.70 ± 0.20	3.52 ± 0.79	< 204	< 77	135 ± 18	45 ± 12
GS+53.18148−27.76950	7.4326	MJS_1180	−18.80 ± 0.20	4.87 ± 1.21	< 293	< 82	204 ± 62	< 59
GN+189.27524+62.21244	7.4318	MJN_1181	−19.29 ± 0.14	7.81 ± 1.20	< 249	< 41	155 ± 43	24 ± 7
GS+53.16746−27.77201	7.2752	DHS_1210	−16.96 ± 0.36	1.78 ± 0.50	134 ± 20	90 ± 29	214 ± 28	146 ± 45
GS+53.16959−27.73805	7.2430	MHS_1180	−20.28 ± 0.08	17.81 ± 1.66	500 ± 89	34 ± 7	< 170	< 15
GS+53.18674−27.77064	7.2425	MJS_1180	−18.23 ± 0.44	< 2.52	204 ± 56	< 659	< 241	< 45
GS+53.16555−27.77267	7.2387	MJS_1180	−18.71 ± 0.27	< 3.01	162 ± 52	< 94	< 116	< 174
GS+53.07543−27.85520	7.2175	MJS_1286	−19.05 ± 0.20	< 2.63	440 ± 65	< 338	–	–
GS+53.11776−27.90701	7.1087	DJS_1287	−18.42 ± 0.11	3.11 ± 0.43	102 ± 23	40 ± 11	223 ± 39	88 ± 20
GN+189.20377+62.26843	7.0897	MJN_1181	−18.99 ± 0.16	4.19 ± 1.32	936 ± 68	278 ± 92	954 ± 41	283 ± 90
GN+189.09630+62.24797	7.0874	MJN_1181	−18.68 ± 0.25	< 3.58	218 ± 64	< 96	< 137	< 52
GN+189.17975+62.28239	7.0850	MHN_1181	−20.09 ± 0.09	12.69 ± 1.64	705 ± 88	69 ± 12	822 ± 100	80 ± 14
GN+189.17253+62.24054	7.0003	MJN_1181	−18.75 ± 0.26	< 4.03	747 ± 75	< 298	–	–
GN+189.20260+62.27551	6.9070	MHN_1181	−19.80 ± 0.06	17.77 ± 0.94	414 ± 45	30 ± 4	298 ± 68	21 ± 5
GS+55.14555−27.78380	6.8782	MJS_1180	−20.06 ± 0.10	18.96 ± 1.68	425 ± 92	29 ± 7	< 243	< 136

Table B1 – *continued*

ID JADES-	z_{sys}	Tier	M_{UV}	$S_C(\lambda_{Ly\alpha,obs})$ 10^{-21} erg s^{-1} cm^{-2} Å^{-1}	$F_{Ly\alpha,R100}$ 10^{-20} erg s^{-1} cm^{-2}	REW$_{Ly\alpha,R100}$ Å	$F_{Ly\alpha,R1000}$ 10^{-20} erg s^{-1} cm^{-2}	REW$_{Ly\alpha,R1000}$ Å
GN+189.15531+62.28647	6.8089	MJN.1181	-20.04 ± 0.05	19.71 ± 1.16	303 ± 66	20 ± 4	461 ± 57	30 ± 4
GN+189.15197+62.25964	6.7590	MHN.1181	-19.83 ± 0.08	12.09 ± 1.21	422 ± 68	45 ± 8	552 ± 88	59 ± 11
GN+189.17514+62.28226	6.7330	MHN.1181	-20.03 ± 0.05	25.09 ± 1.04	879 ± 49	45 ± 3	835 ± 82	43 ± 5
GS+53.15579−27.81520	6.7122	DHS.1210	-18.31 ± 0.13	3.57 ± 0.63	149 ± 27	54 ± 14	316 ± 50	114 ± 27
GN+189.09145+62.22810	6.6740	MHN.1181	-18.93 ± 0.19	9.92 ± 1.84	280 ± 81	< 38	327 ± 78	43 ± 13
GN+189.14579+62.27332	6.6620	MJN.1181	-18.80 ± 0.18	9.36 ± 1.28	< 306	< 51	237 ± 67	33 ± 10
GN+189.24892+62.24974	6.6554	MJN.1181	> -18.39	< 4.64	256 ± 71	< 1467	< 204	< 223
GS+53.16904−27.77884	6.6306	DHS.1210	-18.69 ± 0.05	6.73 ± 0.48	204 ± 21	40 ± 5	212 ± 34	41 ± 7
GS+53.17063−27.74325	6.6247	MHS.1180	-18.94 ± 0.28	< 5.05	420 ± 100	< 299	< 302	< 206
GS+53.13742−27.76521	6.6236	MJS.1286	-19.33 ± 0.10	14.98 ± 1.60	363 ± 72	32 ± 7	471 ± 46	41 ± 6
GS+53.08036−27.89598	6.4737	DJS.1287	-18.34 ± 0.09	4.37 ± 0.41	309 ± 17	95 ± 10	277 ± 30	85 ± 12
GS+53.13492−27.77271	6.3343	DHS.1210	-20.08 ± 0.02	24.76 ± 0.67	733 ± 29	40 ± 2	813 ± 41	45 ± 3
GS+53.19404−27.80293	6.3317	MJS.1180	-18.48 ± 0.23	< 4.18	297 ± 78	< 159	< 203	< 83
GS+53.17836−27.80098	6.3260	MHS.1180	-18.82 ± 0.26	< 7.44	596 ± 106	< 188	< 262	< 426
GN+189.16215+62.26381	6.3120	MHN.1181	-19.39 ± 0.08	11.73 ± 1.26	< 194	< 24	281 ± 65	33 ± 8
GS+53.16611−27.77204	6.3067	MJS.1286	-18.44 ± 0.23	3.77 ± 1.09	501 ± 49	183 ± 57	530 ± 58	193 ± 60
GS+53.16902−27.80079	6.2432	MHS.1180	-18.91 ± 0.22	< 4.31	350 ± 72	< 246	< 267	< 167
GS+53.08604−27.74760	6.2040	MHS.1180	-19.14 ± 0.20	< 5.34	463 ± 97	< 270	< 202	< 202
GS+53.04881−27.87750	6.0507	MJS.1286	-18.89 ± 0.17	6.86 ± 1.74	487 ± 71	100 ± 28	639 ± 84	131 ± 38
GS+53.19588−27.76843	6.0480	MHS.1180	-18.41 ± 0.30	9.46 ± 2.64	< 310	< 53	247 ± 66	< 43
GN+189.10818+62.24715	6.0478	MJN.1181	-18.93 ± 0.13	12.32 ± 1.63	304 ± 61	35 ± 8	< 291	< 57
GS+53.07281−27.84584	5.9945	DJS.1287	-18.95 ± 0.05	8.25 ± 0.60	151 ± 26	26 ± 5	151 ± 44	26 ± 8
GS+53.11052−27.79849	5.9849	DJS.3215	-16.18 ± 0.31	< 0.59	128 ± 8	< 403	128 ± 27	< 462
GS+53.16062−27.77161	5.9734	DHS.1210	-18.55 ± 0.06	6.60 ± 0.56	323 ± 20	70 ± 7	236 ± 40	51 ± 10
GS+53.16692−27.81033	5.9422	DJS.3215	> -16.43	< 0.64	73 ± 11	< 2142	< 127	< 1296
GS+53.11041−27.80892	5.9362	DHS.1210	-18.66 ± 0.05	9.58 ± 0.47	292 ± 16	44 ± 3	313 ± 47	47 ± 7
GN+189.14972+62.22212	5.9361	MJN.1181	-17.95 ± 0.44	< 4.53	673 ± 64	< 785	428 ± 136	< 536
GS+53.12175−27.79763	5.9361	DHS.1210	-19.63 ± 0.02	10.20 ± 0.52	1125 ± 25	159 ± 9	1044 ± 57	147 ± 11
GS+53.15217−27.76817	5.9318	MJS.1180	> -17.93	< 2.40	142 ± 47	< 2296	< 285	< 146
GS+53.15420-27.80551	5.9276	DJS.3215	-16.40 ± 0.44	1.82 ± 0.49	46 ± 15	< 47	< 138	< 112
GS+53.15444−27.77332	5.9220	MJS.1180	> -17.24	< 4.40	143 ± 38	< 230	–	–
GS+53.14077−27.80218	5.9161	MJS.1180	-19.31 ± 0.11	12.93 ± 1.70	285 ± 71	32 ± 9	< 285	< 30
GS+53.16280-27.76084	5.9155	MHS.1180	-19.79 ± 0.10	19.50 ± 2.47	1517 ± 98	113 ± 16	530 ± 62	39 ± 7
GS+53.16773−27.76816	5.9118	MHS.1180	-18.05 ± 0.34	6.68 ± 2.16	< 336	< 73	246 ± 68	< 68
GS+53.17655−27.77111	5.8889	DHS.1210	-18.62 ± 0.10	11.64 ± 1.09	700 ± 37	87 ± 9	< 412	< 20
GS+53.16577−27.80345	5.8848	MJS.1286	-18.83 ± 0.15	4.35 ± 1.21	192 ± 55	< 81	401 ± 100	< 151
GS+53.17986−27.80828	5.8348	MJS.1180	-18.35 ± 0.27	5.76 ± 1.69	289 ± 55	< 78	< 269	< 140
GS+53.16685−27.80413	5.8311	DJS.3215	-18.56 ± 0.07	5.34 ± 0.67	184 ± 31	51 ± 11	< 241	< 34
GS+53.11351−27.77284	5.8141	DHS.1210	-18.13 ± 0.07	5.95 ± 0.52	608 ± 17	150 ± 14	411 ± 70	101 ± 19
GS+53.12210-27.80429	5.7881	DJS.3215	-17.97 ± 0.08	6.14 ± 0.52	160 ± 17	38 ± 5	184 ± 49	44 ± 12
GS+53.05313−27.87897	5.7792	MJS.1286	-18.41 ± 0.23	12.10 ± 2.01	794 ± 61	97 ± 18	–	–
GS+53.13184−27.77377	5.7789	DJS.3215	-18.52 ± 0.04	7.84 ± 0.33	418 ± 11	79 ± 4	364 ± 35	68 ± 7
GS+53.11002−27.85416	5.7784	DJS.1287	-17.53 ± 0.22	2.96 ± 0.79	111 ± 26	< 58	< 206	< 33

Table B1 – *continued*

ID JADES-	z_{sys}	Tier	M_{UV}	$S_C(\lambda_{Ly\alpha,obs})$ 10^{-21} erg s^{-1} cm^{-2} Å^{-1}	$F_{Ly\alpha,R100}$ 10^{-20} erg s^{-1} cm^{-2}	$REW_{Ly\alpha,R100}$ Å	$F_{Ly\alpha,R1000}$ 10^{-20} erg s^{-1} cm^{-2}	$REW_{Ly\alpha,R1000}$ Å
GS+53.13600-27.79849	5.7776	MJS_1180	-18.82 ± 0.17	15.95 ± 1.64	428 ± 64	40 ± 7	475 ± 105	44 ± 11
GS+53.16713-27.79424	5.7734	MHS_1180	> -18.23	6.42 ± 2.06	250 ± 75	< 76	< 335	< 63
GN+189.09179+62.25374	5.7719	MHN_1181	-18.97 ± 0.16	23.54 ± 2.28	432 ± 81	27 ± 6	< 472	< 23
GS+53.15624-27.83617	5.7656	MJS_1286	-19.02 ± 0.16	11.53 ± 2.28	802 ± 83	103 ± 23	941 ± 170	120 ± 32
GS+53.13580-27.76591	5.7612	DJS_3215	-16.87 ± 0.21	< 0.79	98 ± 12	< 318	< 125	< 93
GS+53.06316-27.87341	5.7390	MJS_1286	-18.64 ± 0.20	< 4.84	582 ± 70	< 283	392 ± 90	< 210
GS+53.17350-27.82507	5.6090	MJS_1286	-18.06 ± 0.34	< 3.79	402 ± 59	< 659	392 ± 128	< 687
GN+189.13724+62.26064	5.6000	MHN_1181	-19.41 ± 0.11	20.44 ± 2.54	428 ± 84	32 ± 7	< 642	< 39
GS+53.06512-27.84905	5.5928	DJS_1287	-16.86 ± 0.27	< 1.07	123 ± 14	< 231	< 187	< 124
GS+53.11357-27.82849	5.5783	MJS_1286	> -17.96	< 7.56	759 ± 73	< 188	< 927	< 142
GS+53.14022-27.78709	5.5219	MJS_1286	-18.62 ± 0.22	< 4.98	327 ± 57	< 124	402 ± 133	< 71
GS+53.14565-27.80150	5.5217	DJS_3215	-16.59 ± 0.30	< 1.04	162 ± 12	< 261	–	–
GS+53.06055-27.84840	5.4972	MJS_1286	-18.33 ± 0.26	5.04	997 ± 82	< 1037	1161 ± 159	< 1305
GN+189.10968+62.29506	5.4839	MHN_1181	-19.48 ± 0.13	15.98 ± 2.60	361 ± 95	35 ± 11	< 875	< 44
GS+53.12819-27.78769	5.4817	MHS_1180	-18.22 ± 0.34	12.44 ± 3.52	375 ± 108	< 56	< 705	< 187
GS+53.13859-27.79025	5.4816	MJS_1286	-18.45 ± 0.35	14.63 ± 3.85	1037 ± 126	102 ± 29	< 761	< 208
GS+53.16570-27.78494	5.4716	MJS_1180	-17.79 ± 0.40	< 6.73	< 239	< 55	1021 ± 272	< 300
GS+53.21484-27.79458	5.4040	MJS_1286	-19.20 ± 0.10	18.91 ± 2.23	358 ± 72	30 ± 7	< 522	< 21
GN+189.23015+62.22080	5.4004	MJN_1181	-18.90 ± 0.24	< 6.66	629 ± 101	< 316	< 996	< 162
GS+53.15584-27.76672	5.3500	DJS_3215	-18.57 ± 0.04	8.18 ± 0.42	102 ± 15	20 ± 3	287 ± 77	55 ± 15
GS+53.10590-27.89486	5.3183	MJS_1286	> -18.07	< 8.49	263 ± 73	< 269	< 594	< 5
GS+53.14837-27.74662	5.2914	MJS_1180	-18.30 ± 0.23	6.98 ± 1.60	411 ± 51	94 ± 24	< 618	< 14
GN+189.11532+62.23410	5.1790	MHN_1181	-19.00 ± 0.10	16.74 ± 1.58	750 ± 48	73 ± 8	< 700	< 46
GN+189.25460+62.23668	5.0917	MJN_1181	-19.18 ± 0.20	28.53 ± 4.96	1040 ± 149	60 ± 13	< 1808	< 1516
GS+53.09753-27.90126	5.0782	MJS_1286	-18.90 ± 0.12	14.68 ± 1.85	246 ± 59	27 ± 7	< 1032	< 248
GS+53.11535-27.77289	5.0765	DHS_1210	-19.44 ± 0.05	20.54 ± 1.27	186 ± 42	15 ± 3	< 894	< 34
GS+53.14946-27.80979	5.0520	DHS_1210	-17.92 ± 0.14	7.98 ± 0.79	204 ± 22	42 ± 6	< 1047	< 96
GN+189.02753+62.25374	5.0169	MHN_1181	-18.89 ± 0.13	22.20 ± 2.46	1291 ± 68	96 ± 12	< 1553	< 121
GS+53.19662-27.80531	4.9582	MJS_1180	> -17.89	< 8.99	212 ± 62	< 99	< 2678	< 110
GS+53.16091-27.80354	4.9510	DJS_3215	-17.31 ± 0.31	< 2.62	244 ± 33	< 521	–	–
GN+189.14179+62.25841	4.9410	MHN_1181	-19.46 ± 0.12	32.24 ± 4.06	667 ± 111	35 ± 7	< 3098	< 88
GS+53.12103-27.81599	4.9296	DJS_3215	-18.23 ± 0.06	11.46 ± 0.58	450 ± 16	65 ± 4	< 1937	< 453
GS+53.21033-27.78916	4.9220	MHS_1180	> -18.80	< 25.28	4797 ± 253	< 1081	< 4659	< 471
GS+53.08250-27.84946	4.8960	DJS_1287	> -16.68	3.52 ± 1.13	247 ± 26	< 120	< 1087	< 58
GS+53.18539-27.80073	4.8388	MJS_1286	> -17.87	< 6.55	318 ± 67	< 574	< 2357	< 229
GS+53.13613-27.80399	4.8080	MJS_1286	-18.13 ± 0.31	10.56 ± 2.84	659 ± 83	108 ± 33	< 3034	< 52
GS+53.11237-27.75960	4.7791	MHS_1180	-19.08 ± 0.16	22.04 ± 3.69	397 ± 114	32 ± 11	< 4404	< 306
GS+53.15817-27.78648	4.7742	MJS_1180	-20.25 ± 0.03	64.73 ± 2.25	703 ± 69	19 ± 2	< 2173	< 256
GS+53.12739-27.78524	4.7562	MHS_1180	-18.73 ± 0.23	21.45 ± 4.96	893 ± 147	72 ± 21	< 1274	< 107
GS+53.08773-27.87124	4.7425	MJS_1286	> -17.77	< 6.25	403 ± 106	< 3516	< 2783	< 6590
GS+53.16948-27.76566	4.6870	MJS_1286	-18.46 ± 0.16	18.54 ± 2.35	1381 ± 66	127 ± 17	< 2723	< 151
GN+189.12252+62.29285	4.6819	MJN_1181	> -18.31	< 12.84	1452 ± 145	< 418	< 4583	< 3733
GS+53.13284-27.80186	4.6480	DHS_1210	-18.56 ± 0.05	15.65 ± 0.78	163 ± 24	18 ± 3	< 2488	< 320
GS+53.11958-27.89815	4.6346	DJS_1287	-18.42 ± 0.11	14.89 ± 1.46	503 ± 58	60 ± 9	< 4778	$< nan$
GS+53.11392-27.80620	4.5472	DJS_3215	-20.22 ± 0.01	85.49 ± 1.41	1402 ± 40	30 ± 1	< 1869	< 43

Table B1 – *continued*

ID JADES-	z_{sys}	Tier	M_{UV}	$S_C(\lambda_{Ly\alpha,obs})$ 10^{-21} erg s^{-1} cm^{-2} Å^{-1}	$F_{Ly\alpha,R100}$ 10^{-20} erg s^{-1} cm^{-2}	$REW_{Ly\alpha,R100}$ Å	$F_{Ly\alpha,R1000}$ 10^{-20} erg s^{-1} cm^{-2}	$REW_{Ly\alpha,R1000}$ Å
GN+189.12052+62.30317	4.5350	MHN_1181	-19.64 ± 0.04	37.07 ± 2.56	792 ± 82	39 ± 5	< 3070	< 98
GS+53.16264−27.80368	4.5258	DJS_3215	-18.27 ± 0.05	17.34 ± 0.98	1165 ± 27	121 ± 8	< 3099	< 76
GS+53.16083−27.80455	4.4907	DHS_1210	-18.19 ± 0.13	17.19 ± 1.96	285 ± 52	30 ± 7	–	–
GS+53.16743−27.77585	4.4690	DJS_3215	-16.90 ± 0.16	1.93 ± 0.63	94 ± 21	< 99	< 2705	< 621
GS+53.14700−27.81303	4.4646	DHS_1210	-16.85 ± 0.19	< 2.41	288 ± 27	< 272	< 1550	< 2974
GS+53.06169−27.87309	4.4306	MJS_1286	-18.60 ± 0.12	24.39 ± 3.04	597 ± 85	45 ± 9	< 2939	< 142
GS+53.15294−27.82658	4.4300	MJS_1180	-17.16 ± 0.50	< 9.07	331 ± 65	< 234	< 1856	< 40
GS+53.14936−27.81704	4.4300	DJS_3215	-18.03 ± 0.05	16.41 ± 0.68	125 ± 17	14 ± 2	< 1277	< 167
GS+53.04050−27.87520	4.4290	MJS_1286	-17.81 ± 0.23	13.22 ± 2.75	405 ± 71	57 ± 15	< 3121	< 166
GS+53.20020−27.75714	4.3910	MJS_1286	-17.48 ± 0.31	< 6.11	384 ± 63	< 237	< 2139	< 62
GS+53.08528−27.85042	4.3693	MJS_1286	> -17.37	< 8.23	290 ± 67	< 33471	< 8687	< 848
GS+53.12290-27.81225	4.3110	DJS_3215	-17.29 ± 0.14	2.16 ± 0.69	198 ± 24	< 170	< 3173	< 2230
GS+53.13228−27.79811	4.2830	DHS_1210	> -16.42	< 2.71	171 ± 29	< 833	< 2174	< 41
GS+53.15832−27.80724	4.2331	DHS_1210	-19.05 ± 0.05	36.58 ± 2.09	674 ± 53	35 ± 3	–	–
GS+53.15765−27.79791	4.2279	DJS_3215	-19.28 ± 0.01	33.05 ± 1.32	1184 ± 40	68 ± 4	< 3618	< 381
GS+53.13850−27.80681	4.2246	MJS_1180	-17.15 ± 0.34	6.72 ± 1.99	251 ± 57	< 80	< 8027	< 507
GN+189.25074+62.21889	4.2123	MJN_1181	-18.39 ± 0.18	29.33 ± 5.24	715 ± 112	47 ± 11	< 1551	< 53
GS+53.16496−27.77375	4.2071	MHS_1180	-17.69 ± 0.29	19.93 ± 4.21	742 ± 99	71 ± 18	< 2828	< 62
GS+53.16302−27.77111	4.1562	DJS_3215	-16.80 ± 0.32	9.15 ± 1.90	394 ± 40	84 ± 19	< 3431	< 63
GS+53.17842−27.82131	4.1420	MJS_1286	-19.12 ± 0.07	33.45 ± 4.50	482 ± 156	< 29	< 4393	< 275
GN+189.19740+62.17723	4.1330	MJN_1181	-18.86 ± 0.08	27.29 ± 4.93	2648 ± 166	189 ± 36	< 10254	< 173
GS+53.09292−27.77619	4.1190	MHS_1180	-17.49 ± 0.40	< 14.40	709 ± 141	< 268	< 6750	< 478
GS+53.07374−27.85905	4.0731	MJS_1286	> -17.52	< 17.84	619 ± 145	< 2170	< 3691	< 42
GN+189.19929+62.27946	4.0709	MJN_1181	-17.50 ± 0.31	< 9.23	269 ± 79	< 109	< 4300	< 110
GN+189.19328+62.25373	4.0610	MHN_1181	-20.20 ± 0.03	98.08 ± 4.71	1068 ± 127	21 ± 3	< 8916	< 395
GN+189.18525+62.23876	4.0501	MJN_1181	-18.56 ± 0.10	18.51 ± 2.83	245 ± 76	< 26	< 2353	< 245
GS+53.15548−27.80388	4.0448	DHS_1210	-18.61 ± 0.06	36.07 ± 2.12	519 ± 68	28 ± 4	< 2331	< 616
GS+53.18149−27.82922	4.0370	MJS_1286	-17.18 ± 0.37	< 7.81	658 ± 83	< 311	< 1779	< 25
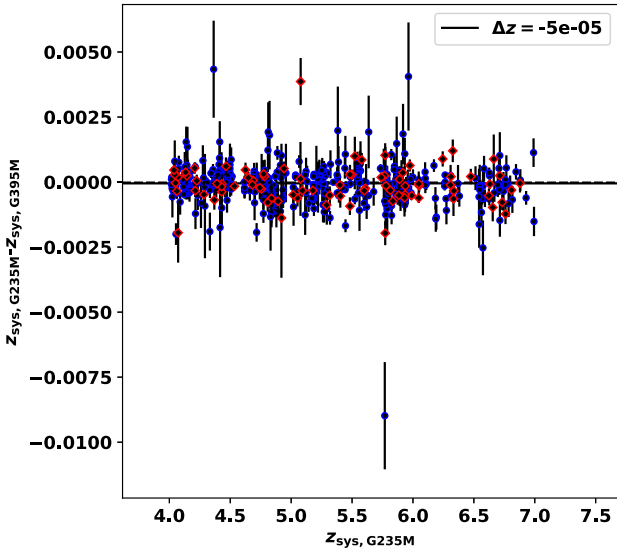
Figure C2. Comparison of redshifts derived from the [O III]λλ4959, 5007–Hβ complex (G235M) and the Hα–[N II]λλ6548, 6584 complex (G395M). LAEs and non-LAEs are shown with red and blue outlines, respectively. The average deviation is listed.

$0.89^{+0.04}_{-0.06}$, which is $\sim 2\sigma$ higher than the estimate using the Nakane et al. (2024) model grid.

[1]*Department of Physics, University of Oxford, Denys Wilkinson Building, Keble Road, Oxford OX1 3RH, UK*
[2]*Kavli Institute for Cosmology, University of Cambridge, Madingley Road, Cambridge CB3 0HA, UK*
[3]*Cavendish Laboratory, University of Cambridge, 19 JJ Thomson Avenue, Cambridge CB3 0HE, UK*
[4]*Department of Physics and Astronomy, University College London, Gower Street, London WC1E 6BT, UK*
[5]*Centro de Astrobiología (CAB), CSIC–INTA, Cra. de Ajalvir Km. 4, Torrejón de Ardoz, E-28850 Madrid, Spain*
[6]*European Space Agency (ESA), European Space Astronomy Centre (ESAC), Camino Bajo del Castillo s/n, Villanueva de la Cañada, E-28692 Madrid, Spain*
[7]*European Space Agency, ESA/ESTEC, Keplerlaan 1, NL-2201 AZ Noordwijk, the Netherlands*
[8]*School of Physics, University of Melbourne, Parkville, 3010 VIC, Australia*
[9]*ARC Centre of Excellence for All Sky Astrophysics in 3 Dimensions (ASTRO 3D), Canberra 2611, Australia*
[10]*Scuola Normale Superiore, Piazza dei Cavalieri 7, I-56126 Pisa, Italy*
[11]*Sorbonne Université, CNRS, UMR 7095, Institut d'Astrophysique de Paris, 98 bis bd Arago, F-75014 Paris, France*
[12]*Centre for Astrophysics Research, Department of Physics, Astronomy and Mathematics, University of Hertfordshire, Hatfield AL10 9AB, UK*
[13]*Steward Observatory, University of Arizona, 933 N. Cherry Ave., Tucson, AZ 85721, USA*
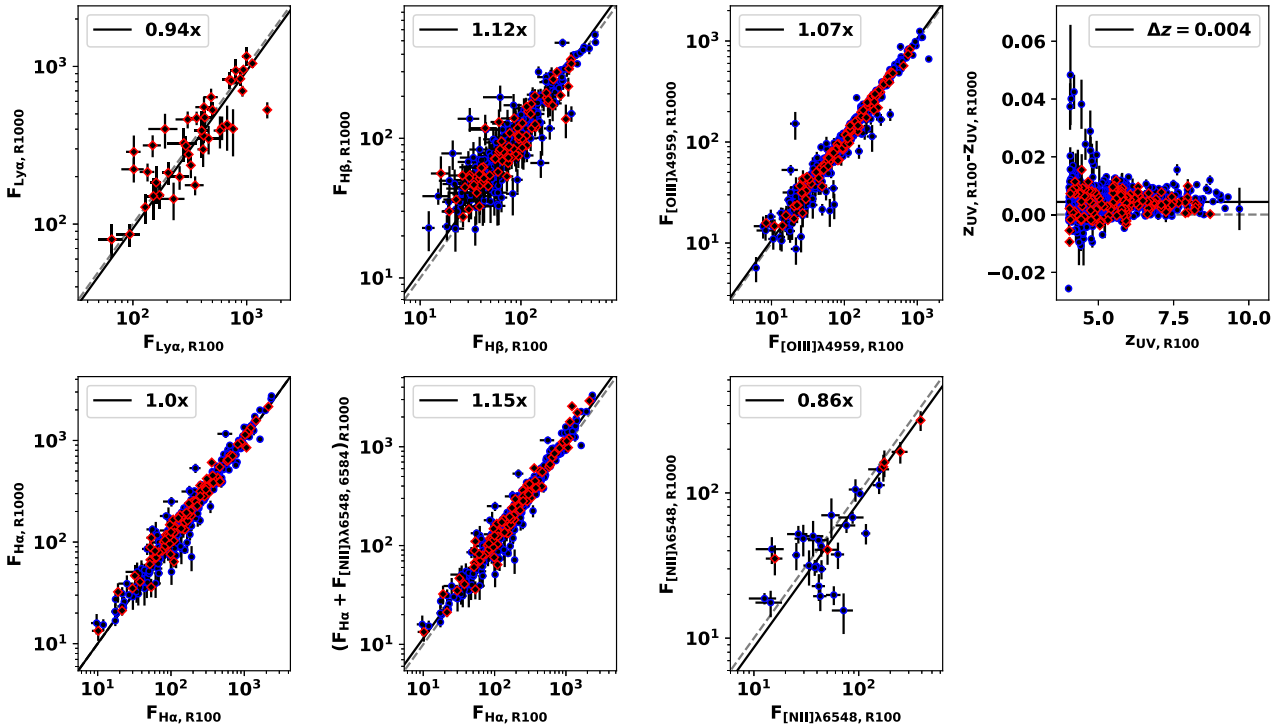
Figure C1. Comparison of line fluxes and spectroscopic redshifts for fits to R100 and R1000 data. We compare fluxes for Lyα, Hβ, [O III]λ4959, Hα, and [N II]λ6548. In addition, we compare the flux of Hα from the R100 data to the combined [N II]–Hα flux of the R1000 fit. The upper right panel shows the difference in spectroscopic redshift derived from the R100 and R1000 data. LAEs and non-LAEs are shown with red and blue outlines, respectively. In each panel, a best-fitting line and its slope (for line flux comparisons) or offset (for redshift comparison) is listed.
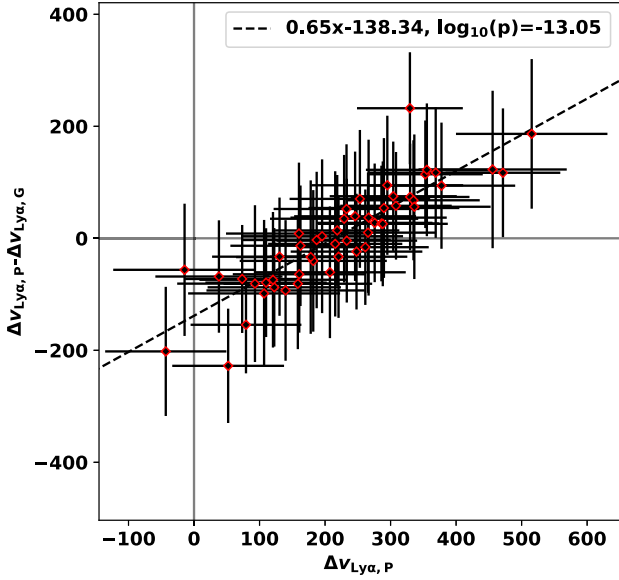
Figure C3. Comparison of Lyα velocity offset derived using two methods: from the centroid of the best-fit Gaussian model ($\Delta v_{Ly\alpha,G}$), and from the highest-flux wavelength within $[-500, +1000]\,\mathrm{km\,s^{-1}}$ of Lyα ($\Delta v_{Ly\alpha,P}$). The best-fitting correlation is shown by a dashed line.

[14]*Center for Astrophysics, Harvard and Smithsonian, 60 Garden St., Cambridge, MA 02138, USA*

[15]*AURA for European Space Agency, Space Telescope Science Institute, 3700 San Martin Drive, Baltimore, MD 21210, USA*

[16]*Department of Astronomy, University of Wisconsin-Madison, 475 N. Charter St., Madison, WI 53706, USA*

[17]*Max-Planck-Institut für Astronomie, Königstuhl 17, D-69117 Heidelberg, Germany*

[18]*Department of Astronomy and Astrophysics, University of California, Santa Cruz, 1156 High Street, Santa Cruz, CA 95064, USA*

[19]*NSF's National Optical-Infrared Astronomy Research Laboratory, 950 North Cherry Avenue, Tucson, AZ 85719, USA*

[20]*NRC Herzberg, 5071 West Saanich Rd, Victoria, BC V9E 2E7, Canada*

This paper has been typeset from a TEX/LATEX file prepared by the author.
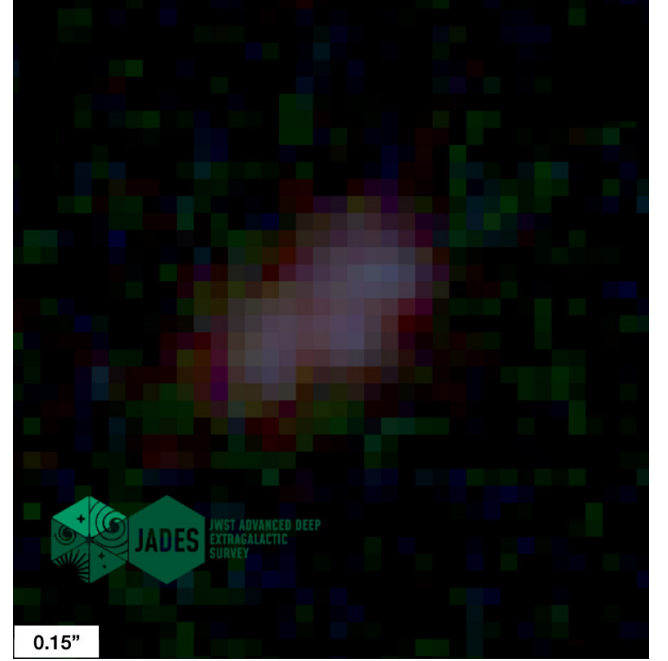
Figure D1. RGB image ($> 3\,\mu m$, $2 - 3\,\mu m$, $< 2\,\mu m$, respectively) created using *JWST*/NIRCam data from JADES observations. The map is centred at $\mathrm{RA} = 53.1374136°$, $\mathrm{Dec} = -27.7652120°$, and a 0.15 arcsec scale bar is shown to the lower left corner. Retrieved from FitsMap (Hausen & Robertson 2022): https://jades.idies.jhu.edu/?ra=53.1374139&dec=-27.7652125&zoom = 12.
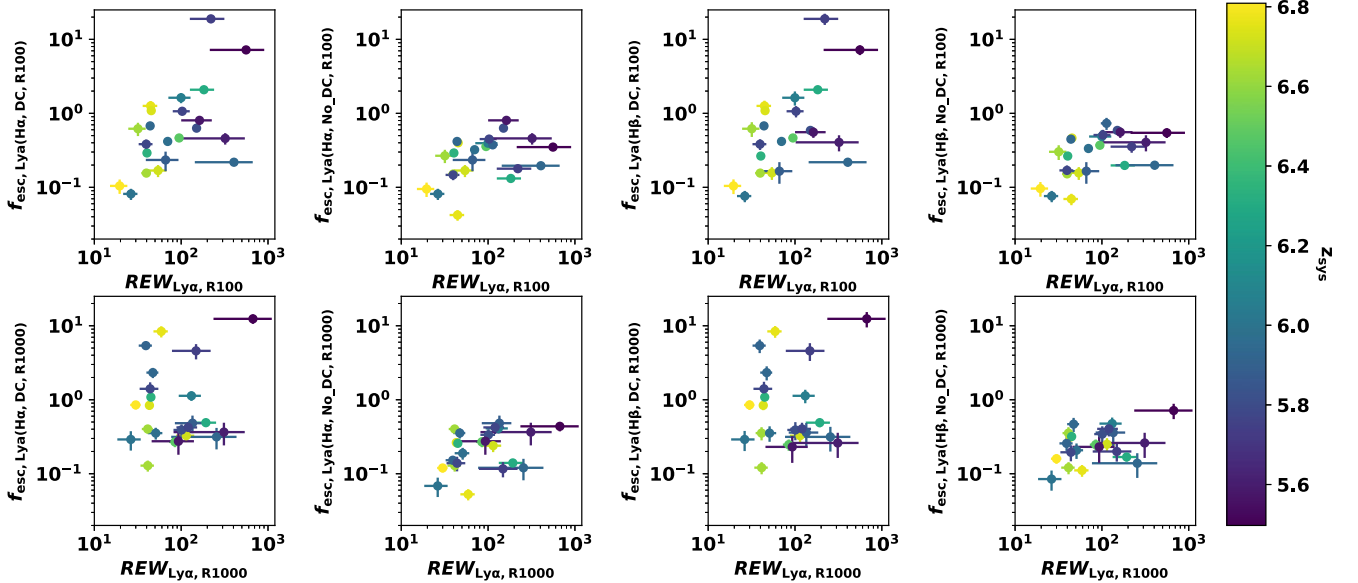
Figure C4. Lyα escape fraction as a function of $REW_{Ly\alpha}$ for a single sample. The upper row shows results from the R100 data, while the lower row shows the R1000 results. In the left four plots, $f_{esc}^{Ly\alpha}$ is derived by comparing the observed and intrinsic Lyα/Hα flux ratio, while the right four plots use the intrinsic Lyα/Hβ flux ratio. The first and third include dust correction, while the second and fourth do not. Points are coloured by redshift.
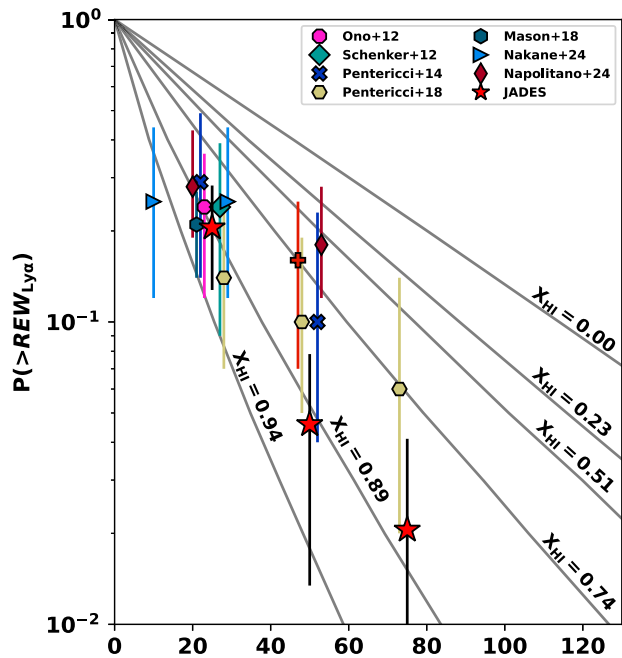
Figure E1. Cumulative distribution for $REW_{Ly\alpha}$ at $z \sim 7$ using galaxies with $-20.25 < M_{UV} < -18.75$, as in Fig. 14. Each solid line shows the expected distribution for a model with $N_{HI} = 10^{20} \, cm^{-2}$, a wind speed of $200 \, km \, s^{-1}$, and an assumed intrinsic $REW_{Ly\alpha}$ distribution scale length of 50 Å, but with a different neutral fraction (Pentericci et al. 2014). Estimates from the literature (Ono et al. 2012; Schenker et al. 2012; Pentericci et al. 2014, 2018; Mason et al. 2018a; Nakane et al. 2024; Napolitano et al. 2024) are shifted by 1 Å for visibility.